

ALPHA FOUNDATION FOR THE IMPROVEMENT OF MINE SAFETY AND HEALTH

Final Technical Report

Project Title: PoroSense: An Intrinsically Safe, Distributed Fiber-optic Gas Sensing Platform for Underground Mines

Grant Number: AFC719-29

Organization: Virginia Polytechnic Institute and State University
Center for Photonics Technology (CPT)
Virginia Center for Coal and Energy Research (VCCER)

Principal Investigator: Yizheng Zhu
Associate Professor
Electrical and Computer Engineering
Virginia Tech

Contact Information : 460 Turner Street, Suite 303 (MC0111)
Blacksburg, VA 24060
Phone: (540) 231-1973
Fax: (540) 231-3362
Email: yizhu1@vt.edu

Period of Performance: 09/01/2018 – 12/01/2020

Acknowledgement/Disclaimer: This study was sponsored by the Alpha Foundation for the Improvement of Mine Safety and Health, Inc. (ALPHA FOUNDATION). The views, opinions and recommendations expressed herein are solely those of the authors and do not imply any endorsement by the ALPHA FOUNDATION, its Directors and staff.

1.0 Executive Summary

Permissibility regulations for gassy underground mines greatly restrict the choice, design and capabilities of gas sensors. There is a strong need for innovative means of permissible gas sensing for safe mine operation, monitoring and characterization.

The proposed research seeks to develop a proof-of-concept, electrically passive, distributed fiber gas sensing platform that can potentially enable a new class of permissible fiber sensors for underground mines. Distributed fiber sensing uses a single, continuous optical fiber¹ to simultaneously detect local environment along the entire length of the fiber (Fig. 1-1) while the system interrogator can be placed at a safe location or even above ground. Such a permissible and flexible system can have important applications in underground mines, such as methane monitoring along longwall faces, in longwall bleeder ventilation systems, at conveyor belt entries, or through mine seals. Fiber sensing systems can also monitor other gas species, such as oxygen and carbon monoxide, as well as physical parameters, such as temperature and pressure.

Although of tremendous interest, distributed fiber gas sensing is perhaps the most challenging distributed sensing subject. Other parameters, such as temperature, strain, pressure, or vibration, have all been commercially available or demonstrated. Distributed gas sensing, however, has yet to see a breakthrough after decades of fiber sensing research.

The challenge is two-fold: (1) lack of distributed gas sensor interrogation techniques and (2) lack of sensing media. To tackle both, we propose (1) novel laser interrogation technique using ultra-short chirp pulses, and (2) novel porous-clad optical sensing fibers. The proposed system is aimed at significantly expanding the intrinsic permissibility and functionality in underground sensing and many other applications alike.

During the course of the project, we have conducted extensive research in the following areas: optical interrogator, porous fiber fabrication and characterization, specialty sensor investigation (off-centered core fiber), and gas sensing evaluation. These efforts are not only experimental, but also theoretical and aided by numerical simulations. An overview of research efforts will be discussed in Fig. 3-1.

Through the project, we have made the following technical accomplishments:

- For the first time, successfully developed an enabling interrogation technique (ultra-short chirp pulses) and demonstrated its feasibility and superior performance, paving the way for distributed fiber gas sensing.
- Fabricated hundreds of meters of novel fibers, demonstrated the sensing potential of the porous-clad fiber sensor and the special off-centered core design at single-sensor level using the new interrogation. Gained extensive insight into the optimal design, fabrication and performance of these and future designs.
- Generated multiple publications, presentations and an M.S. thesis, and supported

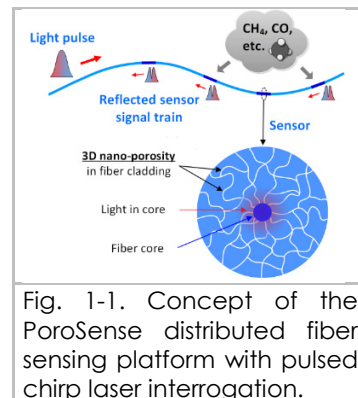


Fig. 1-1. Concept of the PoroSense distributed fiber sensing platform with pulsed chirp laser interrogation.

¹ Optical fiber: Long, hair-thin threads of glass or polymer made to transmit light over extended length. A fiber has two layers of glass – a central “core” and the outer “cladding”. They are such that light is trapped inside and around the core but can travel along the length. See Fig. 1-1. Optical fibers are electrically safe.

multiple graduate students and a postdoc.

- The all optical system implementation and the low light power suggest great potential for permissible applications in underground mines.

We also acknowledge that, in the final stages of the project, the complexity and challenges of the research exceeded previous assessment, and impeded the team from demonstrating the cascaded, multi-point gas sensing within available resources. Although this leaves much to be desired, the research has richly enabled us to gain extensive knowledge of the challenges ahead and identify key focus areas to further advance the proposed technique toward a practical, real-world system that can benefit the improvement of mine safety. One such focus area is the reduction of fiber attenuation. Through this research, we have identified key loss mechanisms and investigated different fiber designs that could ultimately enable the desired long-span distributed sensing.

Finally, we expect the research, its impact and dissemination to strongly continue.

2.0 Problem Statement and Objective

Problem statement: Permissibility regulations for gassy underground mines greatly restrict the choice, design and capabilities of gas sensors. Current devices are primarily electrically powered sensors, posing explosion/fire hazards such as sparks and heating. These challenges arise in all gassy underground mines. There is a clear and strong need for innovative means of permissible gas sensing, which is highly desirable for safe mine operation, monitoring and characterization.

The objectives of this project are to: (1) demonstrate the concept of using porous-clad optical fibers, pulsed laser absorption spectroscopy and spectral self-calibration as a valid means of rapid gas sensing; (2) determine the feasibility of porous-clad fibers as a low-loss medium for long-span distributed sensing; and (3) determine the sensor's performance and permissibility potential.

The long term goal is a permissible distributed fiber-optic sensing system for multi-gas detection and quantification in coal and other underground mines, in order to monitor gas distribution and improve mine operation and the health and safety of miners. More broadly, the system can potentially be used for monitoring other parameters, such as temperature and vibration, to provide crucial sensing capabilities for normal operation as well as escape and rescue.

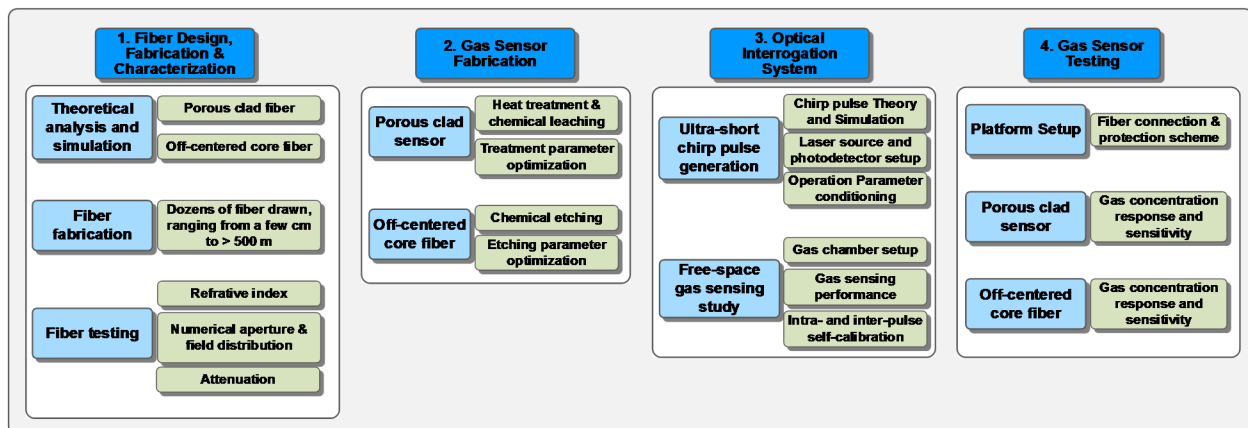


Fig. 3-1. Overview of the research efforts.

3.0 Research Approach

To achieve the distributed gas sensing system, research efforts have been focused on (1) optical fiber design, fabrication and characterization, (2) gas sensor fabrication, (3) development of optical interrogation system, and (4) gas sensor testing. These project efforts are summarized in the high-level diagram in Fig. 3-1.

In the design of optical fiber gas sensors, we investigated two types of gas sensor and their fiber designs, which are based on porous clad fiber and off-centered core fiber, respectively. To obtain suitable fibers capable of sensor fabrication, we explored several glass material combinations currently available for optical fiber. Dozens of fiber samples of both types, as short as a few centimeters to as long as hundreds of meters, were fabricated using the fiber drawing facilities at the Center for Photonics Technology at Virginia Tech. Fig. 3-2 shows part of the fiber collection. Some other structures and geometries will be shown later in this report. With a series of fiber characterization, we decided on BK-7 core/Green Vycor cladding fiber for porous clad sensors and Ge-doped core/fused silica cladding fiber for off-centered core sensors.

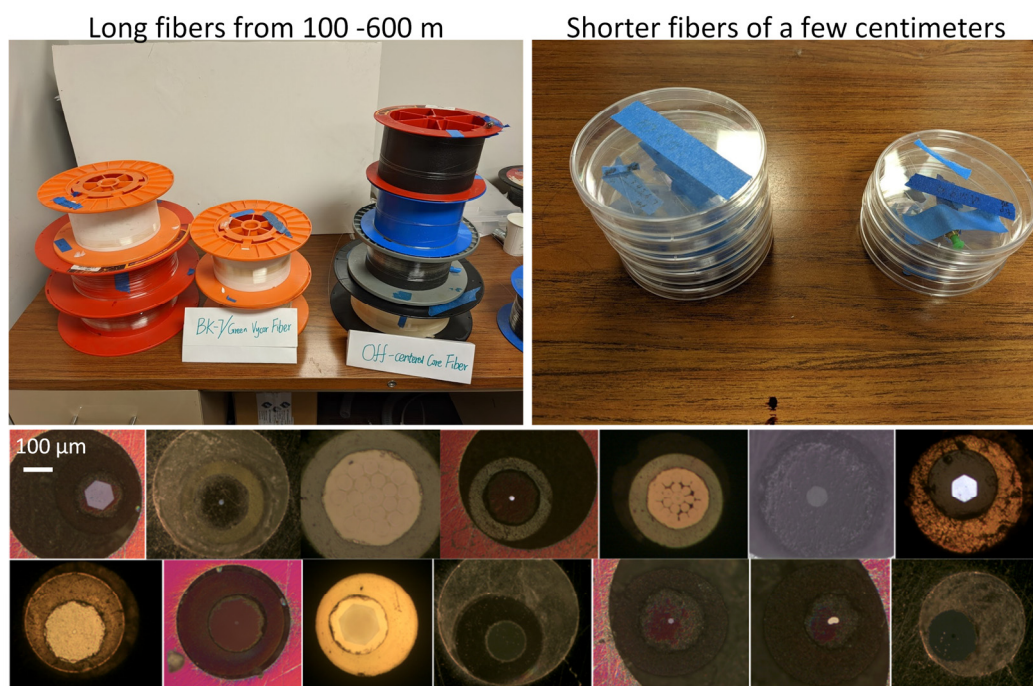


Fig. 3-2. (Top) Partial collection of custom fibers drawn at the Center for Photonics Technology at Virginia Tech for this project, using a variety of materials and geometry to study their optical properties and optimize sensor fabrication parameters. Their length ranges from a few centimeters to >600 m. (Bottom) Cross-section images of some of the fibers. The large or small bright spots at the center are the fiber core. The next layer is the fiber cladding, followed by a polymer coating. The largest circle is the edge of the hole that holds the fiber during polishing. A scale bar is added, representing 100μm. The scale is similar in all images.

With the suitable fibers, porous clad gas sensors and off-centered core sensors were fabricated after a series of chemical and thermal treatments. A numerical model was also designed to simulate the optical field distribution in fiber cross section and guided the design and fabrication of off-centered core sensor.

In the meantime, an optical interrogation system based on frequency chirped pulses

was developed and fully characterized. We also developed a numerical model to simulate the chirped output from a laser diode and determine the best parameters of the interrogation signal.

Finally, several gas sensing systems were setup with free space² transmission spectroscopy, a reference time delay arm³, porous clad sensor and off-centered core sensor. Experimental results confirmed their effectiveness in gas sensing. The free space transmission spectroscopy system achieved methane concentration sensing with a sensitivity of 25 ppm. The system with a reference time delay arm achieved inter-pulse calibrated gas sensing and confirmed the effectiveness of using this system for distributed gas sensing with a spatial resolution of 2 m. Furthermore, with the porous clad sensor, self-calibrated, full range methane concentration sensing was achieved with a good linearity between the measurement and methane concentration and a sensitivity of 100 ppm. The experiments with the off-centered core sensor also confirmed its response to methane concentration and its potential in low attenuation cascaded distributed gas sensing.

3.1. Fiber design, fabrication and characterization

The fiber used for gas sensor fabrication needs to have a balanced performance between optical field exposure (which may increase attenuation because of enhanced interaction with ambient environment) and low attenuation (which may limit the interaction between detection signal and ambient environment). Therefore, the material as well as geometrical parameters of the fiber need to be carefully selected and designed. To meet these requirements, out of the many fibers explored, we chose two types of fiber, one with BK-7 core/ Green Vycor cladding for the fabrication of porous clad fiber; the other type has Ge-doped core/ fused silica cladding for the fabrication of off-centered core fiber.

3.1.1. Design of fiber for sensor fabrication

For the fabrication of porous clad fiber, the cladding section needs to use Green Vycor glass to form porous structures through phase separation and chemical leaching. To maintain light propagation property and suitable numerical aperture (NA)⁴, BK-7 glass was chosen to be the material of core [1] [2]. As a result, the core/cladding material

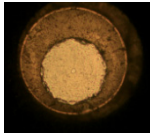
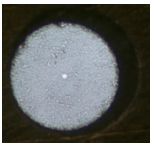
² Free space: Through air or vacuum. Some characterizations were performed for light propagation in air (free space), in particular for interrogator characterization. Non-free space cases are sensor characterization with light inside an optical fiber.

³ Reference arm: A reference arm is a second channel of optical signal created for comparison with the signal channel under investigation (often referred to as "sample arm"). Reference arms are used when a known standard is needed to compare and evaluate the signal from the sample.

⁴ Numerical aperture: A measure of how well a fiber can collect light. A high NA fiber can collect light entering the fiber within a wider range of angles. A multimode fiber has higher NA, thus allowing more possible paths (modes) for light to travel. A singlemode fiber has much smaller NA, thus restricting the number of possible light path to one. The value of NA is decided by the difference in refractive index between core and cladding. Higher difference results in higher NA.

combination for the porous clad fiber was confirmed. As for the fiber for off-centered core sensor, we considered using Ge glass as core material in new design. Commercial fiber with Ge-doped core and two claddings, whose first layer of cladding was F-doped and the second one was fused silica, was tested to have an attenuation of 0.04-0.08dB/m (Table 3-1). The Ge-doped core fiber with fused silica cladding drawn in-house was also measured, and attenuation coefficient was 0.091dB/m (Table 3-1). The low loss showed that the Ge-doped-core fiber with fused silica cladding can transmit light efficiently. However, owing to its simple fabrication procedure and acceptable attenuation coefficient, the Ge-doped core/fused silica combination was sufficient for the off-centered core sensor.

Table 3-1. Transmission microscope images⁵, core size and α of Ge-doped core fiber

	Microscope images	Core size (μm)	Attenuation coefficient α (dB/m)
Ge-dope core/ F-doped cladding/ fused silica cladding		8.78	0.04-0.08
Ge-dope core/ fused silica cladding		8.75	0.091

In conclusion, BK-7/Green Vycor material combination was selected for porous clad sensor and Ge-doped silica/fused silica material combination was selected for off-centered core sensor. A number of batches of fiber samples with different geometrical parameters were fabricated. In order to better understand their properties and determine the best parameters for sensor design, a series of characterizations were performed on these fibers.

3.1.2. Fiber fabrication

As mentioned above, a large number of fiber samples were fabricated using the fiber drawing facility at the Center for Photonics Technology at Virginia Tech. First, the fiber preforms⁶ were fabricated on a glass working lathe and then drawn to 125-250 μm diameter fibers and acrylate coated on a commercial scale fiber draw tower. Figure 3-3(d) shows the cross-sections of one fiber with its entire core and cladding illuminated,

⁵ Transmission microscope image: Taken with a microscope while illuminating the fiber from the other end to examine the fiber core and cladding. Different optical properties in these regions will impact the light differently. Such images help differentiate core/cladding and investigate their properties qualitatively.

⁶ Fiber preform: A large glass rod with the same geometry and composition as the target fiber. The preform is then heated to soften. Pulling on the preform will draw glass fibers into much smaller diameter but with the same geometry and composition.

while in Figs. 3-3(e) and 3-3(f) only the core is illuminated. The multiple layers of cladding in Fig. 3-3(f) is a result of repeated cladding processed to achieve the desired core-to-cladding ratio. While adjustment will be made to improve the core-cladding concentricity, these results have clearly shown that fibers can be produced with very small core diameter ($\sim 10\mu\text{m}$) when needed, which is beneficial for enhancing sensing capability and flexibility.

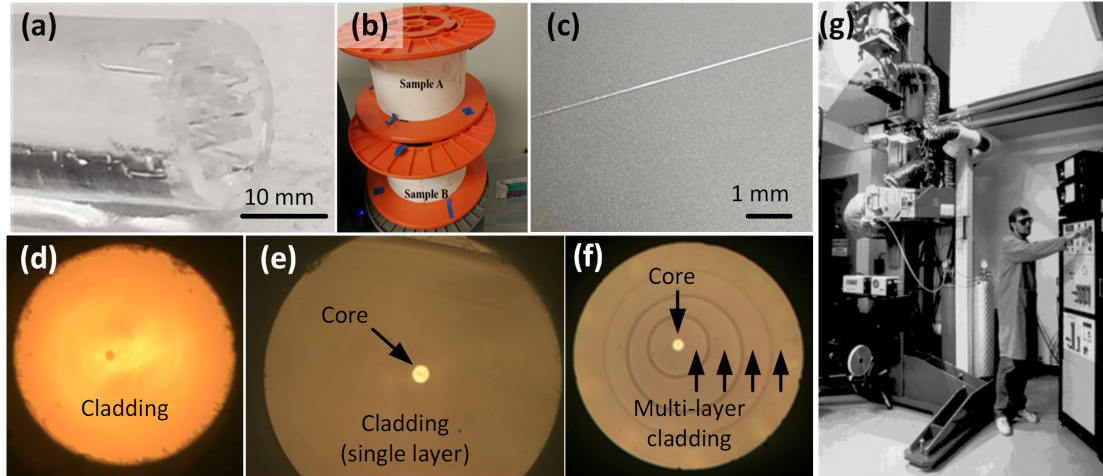


Fig. 3-3. Porous clad fiber fabrication. (a) Fiber preform before drawing. (b) Sample fibers spool after drawing. (c) Drawn fiber with protective coating. (d) Illuminated cladding. (e) Illuminated core. (f) Fiber with a multi-layer cladding structures. (g) Virginia Tech's commercial grade fiber draw tower.

3.1.3. Refractive index measurement

The Ge-doped core/fused silica cladding fiber used commercial fiber glass with well-evaluated properties, so the refractive index (RI)⁷ of the materials are well known [3]. However, the RIs of BK-7 and Green Vycor glass have not been well characterized. In order to better characterize these materials and guide the fabrication of fiber samples, the RIs of BK-7 and Green Vycor were measured. In the measurement, pure glass rods made of BK-7 and Green Vycor were used in the measurement, respectively. The RI measurement system is schematically illustrated in Fig. 3-4, which is based on an optimized Michelson interferometer [4]. A swept laser source with the tuning range of 830-860 nm was used as light source. The sample rod was immersed in refractive index liquid and placed between two cover glasses and formed a sample chip. The sample chip was placed on the sample platform in the sample arm. By sweeping the wavelength of light source and measuring interference images between sample arm and reference arm, the optical path length (OPL) distribution of sample chip can be measured, which can then be transferred into refractive index difference between sample and refractive index liquid. Since the RI of refractive index liquid was known, the RI of these materials can be obtained.

⁷ Refractive index: A measure of how strongly a type of glass or other optical materials can bend (refract) light. In an optical fiber, the refractive index of the core should be higher than that of the cladding in order to trap light inside/near the core. Therefore, it is important to measure the RI of the fiber core and cladding materials.

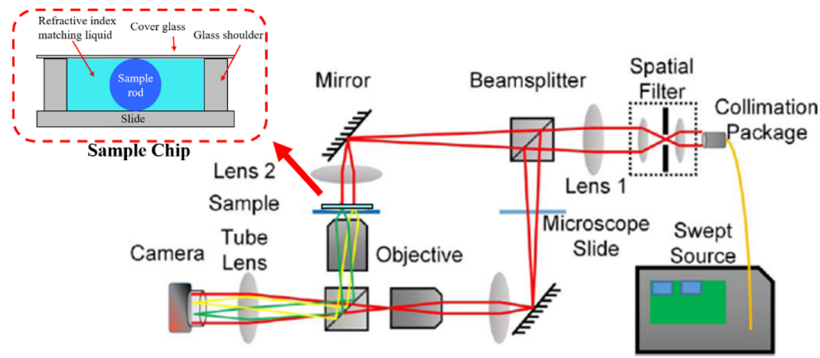


Fig. 3-4. RI measurement system configuration (Inset: structure of sample chip).

To measure the interference images at each output wavelength of the swept source and obtain OPL, a series of measurement control programs and data processing programs were used. The interference image measured from the system as well as OPL measurement interface is shown in Fig. 3-5.

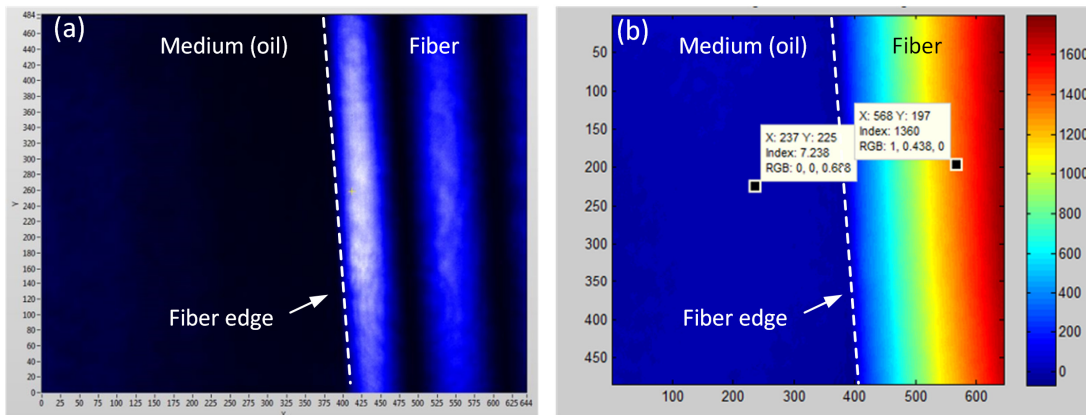


Fig. 3-5. Interference image and optical pathlength measurement for RI determination. (a) Measured interference image of sample. (b) OPL calculation. The position of the fiber and its surrounding medium (oil) are marked.

Using this system, we can accurately measure the RI of each material at ~860 nm band, which is shown in Table 3-2. It can be seen that RI of BK-7 is larger than that of Green Vycor, which indicates BK-7 (core) and Green Vycor (cladding) can form optical fibers.

Table 3-2. RI of the materials

Material	BK-7	Green Vycor
Refractive index	1.495	1.473

3.1.4. Attenuation⁸ measurement

The Ge-doped silica core/fused silica cladding fiber has been proved to show very low attenuation in the determination of glass material for off-centered core sensor, which will

⁸ Attenuation: The loss of light when passing a component, such as a piece of fiber.

not significantly affect the sensor fabrication. Thus, only the attenuation of BK-7/Green Vycor fiber needs to be carefully measured.

The principle of the attenuation measurement system shown in Fig. 3-6 is cut-back method, which derives the result by calculating the ratio of output powers between fibers with different lengths [5]. Laser diode (LD) with a central wavelength at about 1550nm was driven by a temperature controller (TEC) and a current driver. The output was then collimated and coupled to the sample fiber through a free space coupling system (U-bench-system, Thorlabs) and finally detected by a photo detector (PD). The U-bench-system was a five-dimension free space coupling system which can adjust the position and direction of collimated laser output beam to acquire the maximum coupling efficiency.

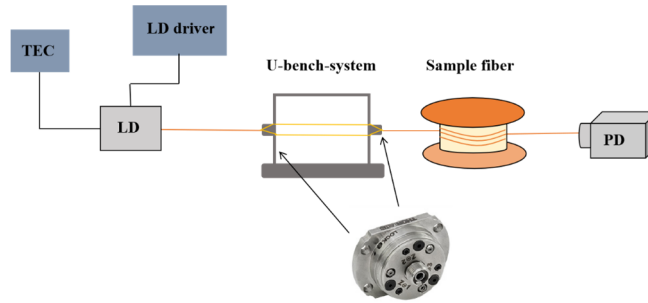
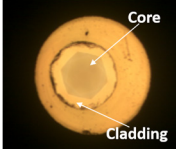
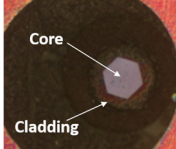
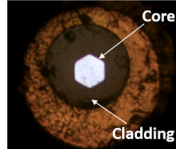
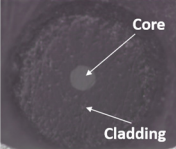
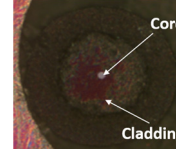


Fig. 3-6. Fiber attenuation measurement system.

Using the system introduced above, attenuation coefficient (α) of BK-7/Green Vycor samples in different core size can be obtained. As shown in Table 3-3, fiber core size varies from 14 μm to 106.2 μm , which includes both singlemode and multimode fibers. Regardless of the core size, the attenuation of these samples is greater than 3dB/m⁹, which is a relatively high value for long distance distributed sensing. A desirable value would be less than 1dB/m for multi-point measurement and a fraction of dB to below 0.1dB for tens of or hundreds of cascaded sensors.

It is believed that fiber impurity, water content, fiber drawing quality are potentially the major causes of such attenuation. After carefully examining these potential causes, the team believe improving fiber/drawing quality, optimizing fiber geometry and enhancing fiber purity (especially water content) can potentially greatly reduce attenuation in future fibers.

Table 3-3. Transmission microscope image, core size and α of all BK-7/Green Vycor samples

Transmission microscope images					
Core size (μm)	106.2	96.5	64.6	30.62	14.00
Attenuation coefficient α (dB/m)	4.2	4.0	4.0	4.6	3.6

⁹ dB (decibel): A relative unit of change. 3dB is equal to a change to 50%. 10dB is equal to a change to 10%.

The attenuation of Ge-doped silica core/fused silica cladding fiber samples were also conducted, which has a much lower attenuation of ~ 0.4 dB/m, corresponding to $> 90\%$ transmission.

3.1.5. Numerical aperture measurement

In the design of the off-centered core sensor, the core/cladding size and coupling with normal singlemode fiber¹⁰ is critical. Therefore, the NA of the fiber for off-centered core sensor should be carefully controlled. Thus, NA measurement experiments were conducted for Ge-doped silica/fused silica fiber [6]. The experimental setup for NA measurement system is schematically shown in Fig. 3-7. A laser diode was used as light source. A chopper was used to modulate the output from fiber sample to increase measurement accuracy. Far-field energy distribution from sample was measured by a scanning photodiode.

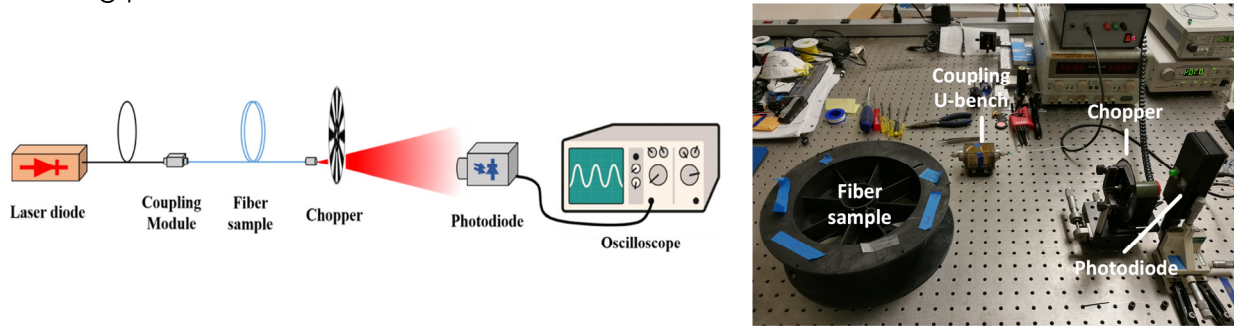


Fig. 3-7. Setup of the numerical aperture measurement system.

In the experiment, two samples with Ge-doped core and fused silica cladding was measured. The far-field energy distribution of samples was captured and fitted with Gaussian function, then the NAs can be calculated with the fitted curve, which is shown in Fig. 3-8.

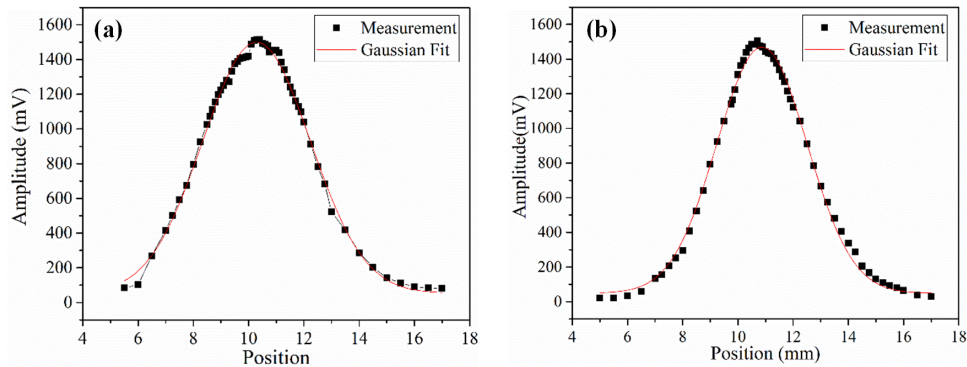


Fig. 3-8. Far field energy distribution from fiber samples. (a) Far-field energy distribution of Sample A; (b) Far-field energy distribution of Sample B.

¹⁰ Singlemode fiber: A common type of optical fiber, where light can only travel along a single path inside the fiber core. This is due to the very small diameter of the core and the small difference in refractive index between the core and the cladding. Both features restrict the possible paths of the light to a single, fundamental pattern. In the contrary, a fiber allowing many difference travel paths of the light is called a multimode fiber.

The NA measurement results for the two samples are shown in Table 3-4. The measurement results showed a low NA value of these fibers. Combining the result with attenuation measurement of ~ 0.4 dB/m, by carefully design of core and cladding parameters, Ge-doped silica glass has the potential to serve as a low attenuation core material for a fiber sample with controllable NA. Comparing the parameters of the two samples, we chose Sample B for the further fabrication of off-centered core sensor. Furthermore, for an easier treatment to fabricate off-centered core sensor, a batch of fibers was fabricated with the same core/cladding materials as Sample B as well as an off-centered core with a core-air gap of $35\text{ }\mu\text{m}$.

Table 3-4. NA measurement of fiber samples

	Max Power Position (mm)	5% Max Power Position (mm)	Distance from Fiber Facet (mm)	NA
SAMPLE A	10.289	15.952	35.685	0.1567
SAMPLE B	10.874	15.547	35.685	0.1298

In summary, after comparison of a number of batches of fibers, we have determined the optimal geometrical parameters of available fibers for further fabrication of sensors. The fiber used for porous clad sensor has BK-7 core/Green Vycor cladding with core/cladding size of $65/160\text{ }\mu\text{m}$, and the fiber used for off-centered core sensor has Ge-doped silica core/fused silica cladding with core/cladding size of $8/140\text{ }\mu\text{m}$ and a core-to-air gap of $\sim 35\text{ }\mu\text{m}$.

3.2. Sensor fabrication

With the determined fiber parameters, both porous clad sensor and off-centered core sensor were fabricated.

3.2.1. Porous clad sensor fabrication

After drawing fibers with Green Vycor glass cladding, we need to conduct heat and chemical treatments to achieve phase separation and porosity formation within cladding section. Through numerous trials using various short and long pieces of fibers, the whole treatment procedure as well as the experimental setup has been optimized multiple times to suit for the treatment of fibers with length suitable for sensors. With this method and setup, we achieved porous clad fiber samples with as long as ~ 70 cm. More than half a dozen of long pieces of fibers ranging from 50 – 70 cm have been fabricated.

Porous clad fiber treatment procedure

The porosity formation treatment procedure in Green Vycor glass is illustrated in Fig. 3-9 [7]. It should be noted that comparing to our original design, the last treatment was changed from dry in air to desiccation by heat to accelerate the evaporation of water in cladding section and avoid blockage of porous channel.

Apart from the optimization of treatment procedure, experimental setups were also improved for the treatment of sample with meter-level length. The experimental setup

was shown in Fig. 3-10. Meter-long level length of fiber sample without coating was placed on a steel heating plate and put into the central heating area of the furnace. A thermocouple was set near the heating plate to get accurate readings of temperature of fiber sample. After heat treatment, the sample was placed in the ring-shape channel of a Teflon container for HF etching. The ring-shape channel was designed to guarantee uniform etching speed and avoid damage to sample caused by bending. Samples after HF etching were placed into a glass container filled with nitric acid for chemical leaching. A heating plate connected with temperature controller was utilized to heat the solution to 80°C and maintain a constant temperature for 18 h. When the leaching process was completed, the sample was immersed in distilled water for sodium-rich-phase dissolution and then desiccated with heat gun.

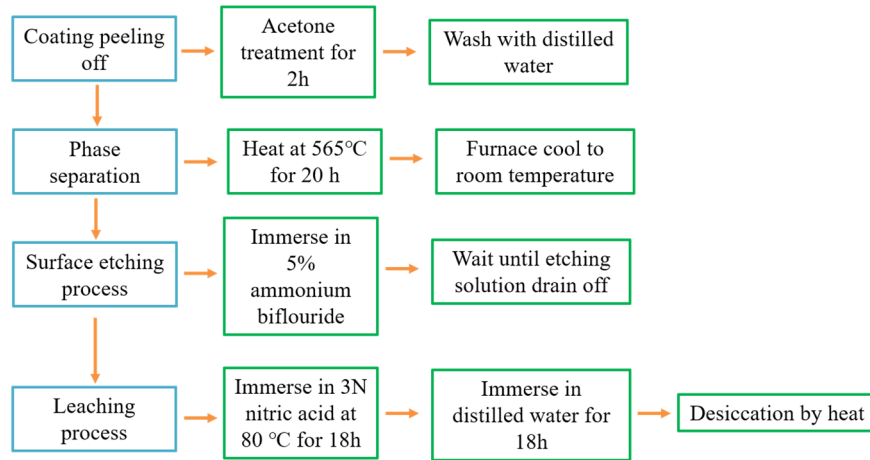


Fig. 3-9. Porosity formation procedure.

As a test of the porosity formation treatment, Green Vycor glass rod with a diameter of 100 μm and fiber with 96.5 μm hexagon BK-7 core and Green Vycor cladding with a 130 μm outer diameter was treated following the procedure mentioned above.

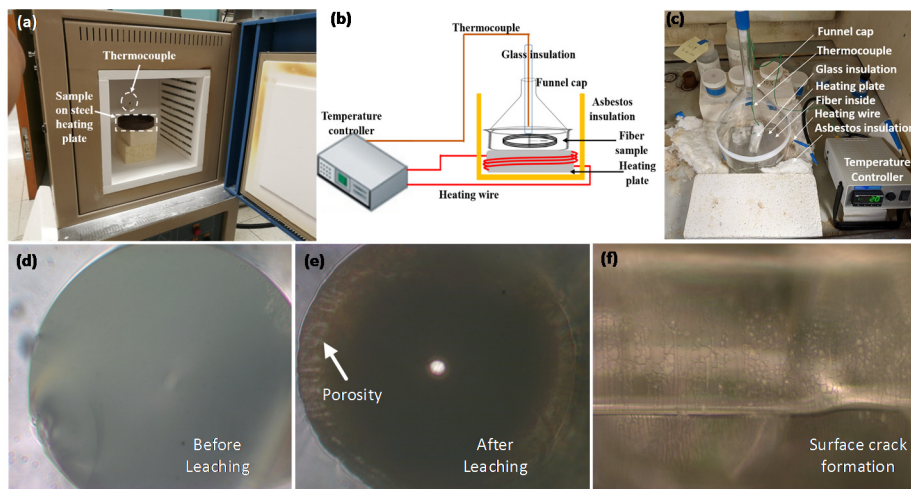


Fig. 3-10. Fiber treatment and porosity formation. (a) New furnace for heat treatment. (b), (c) Chemical leaching setup. (d), (e) Fiber before and after leaching and porosity formation. (f) Surface cracks on porous fiber.

Porosity formation in Green Vycor glass rod

We first tested pure Green Vycor rod for porosity formation using the above treatment. The porosity formation is similar to those presented in Fig. 3-10 (d) and (e). It can be seen from the figure that after treatment, porous structures can be created in Green Vycor glass, which caused opacity and light scattering. Moreover, because of the formation of porosity and strain release, cracks were also observed in the glass rod, as in Fig. 3-10(f), which made the Green Vycor rod prone to break. This has been a challenge for generating porosity through the entire layer of cladding, but off-centered core design can offer significant mitigation.

Porosity formation in fiber with BK-7 core/ Green Vycor cladding

As a further evaluation of porosity formation treatment procedure, fiber sample with BK-7 core and Green Vycor cladding was treated. The microscope images in Fig. 3-11 (a) and (b) show the fiber end surface when it is illuminated from the viewing end (a, reflection) or the other end (b, transmission). In Fig. 3-11(a), the brighter image of the cladding as compared to the core suggests increased light scattering, which is typical for porous structure. In the transmission image of Fig. 3-11 (b), the cladding is darker than the core, also consistent with the fact that porous structure scatters light more so less light reaches the viewing end but the light in the core is low loss and unaffected. Fig. 3-11 (c) shows the surface cracks associated with porosity generation.

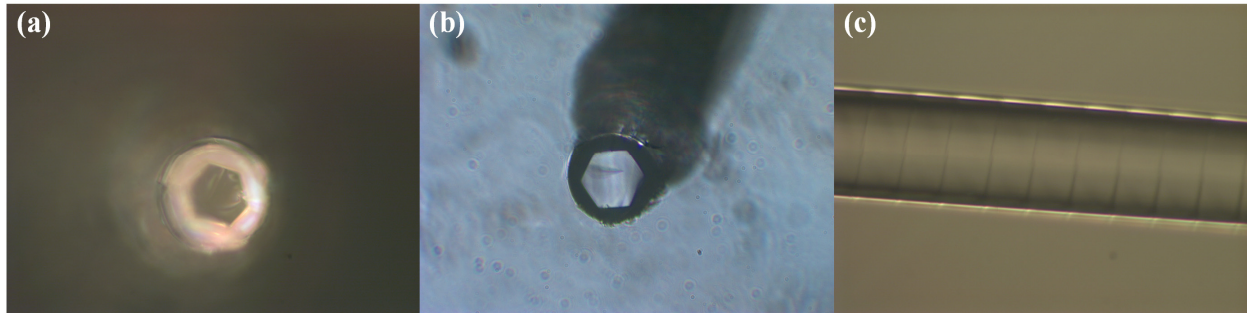


Fig. 3-11. Microscope images of porous-clad fiber sample after porosity formation. (a) Cross-section image by illuminating fiber from viewing end. (b) Cross-section image by illuminating from the other fiber end. (c) Side view image of the fiber shown surface cracks.

Connection between porous clad fiber and silica fiber

Because of the extreme low melting point of BK-7 and Green Vycor glass compared with that of fused silica which is normally used for commercial fiber, it is rather difficult to directly fusion splice the two fibers together as in standard practice. Thus, we used direct alignment of the two fibers through a piece of capillary tubing to maintain high coupling efficiency¹¹ and reduce coupling loss. To match with the core size of porous clad fiber and achieve high coupling efficiency, 62.5/125 μm multimode fiber¹² was used as input

¹¹ Coupling efficiency: The percentage of light from one fiber that is received by another fiber. This parameter is important when different types of fibers need to be connected. High efficiency will ensure low-loss connection.

¹² Multimode fiber: A common type of fiber that allows the light inside the fiber core to travel along many different paths. As compared to a singlemode fiber, a multimode fiber usually features larger core diameter and larger difference in refractive index between the fiber core and fiber cladding.

and output fiber for porous clad sensor. As shown in Fig. 3-12, the two fibers were inserted into a capillary tubing with ID of 180 μm . The position of the two fiber ends were adjusted carefully to obtain the highest coupling efficiency. After the alignment, the two fibers as well as the capillary tubing were bonded to a glass slide with epoxy to keep the joint point stable.

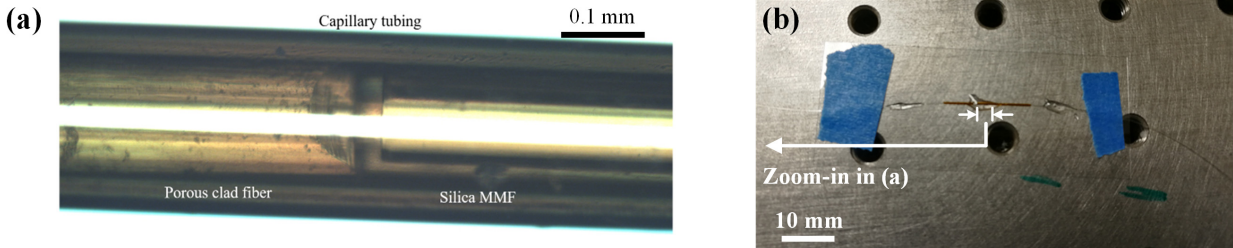


Fig. 3-12. Coupling between porous clad fiber and silica fiber. (a) Alignment between the two fiber ends in capillary tubing; (b) Mounting of fiber on glass slide.

Both the input and output ends of the porous clad fiber were connected to silica fiber in the same way, which provided a stable connection with an energy coupling efficiency of $\sim 60\%$. This value is high considering the different geometry of the two fibers.

In itself, the 60% efficiency for this type of coupling can be considered as very high because the porous-clad fiber and silica fiber are not specifically made to have the same light intensity distribution. Such process is intensive in design and fabrication. When the distributions match, the coupling efficiency can be 90%-95%.

For future fabrication of distributed gas sensors, 60% is not sufficient and will lead to significant loss of power when many sensors are connected. However, we believe this can be solved through the following options:

1. If fiber connection is needed, fusion splicing (melt & join) between porous clad fiber and a regular fiber is difficult. Mechanical splicing should be the choice and the fibers need to be designed/fabricated such that their light distributions match each other.
2. The ultimate approach, we believe, is to have a long, continuous fiber with sensors fabricated directly on the fiber without the need to connect sensors. This will eliminate the connection loss.

At this stage, fiber connection will allow us to investigate individual sensor performance and examine the factors affecting sensor connection.

3.2.2. Sensor based on off-centered core fiber

The aim of using the off-centered core sensor is to expose a portion of the light around the fiber core for interaction with the ambient gas without making the entire cladding porous.

In a traditional circular fiber, the core and its light field are located at the center of the fiber. Therefore channels have to be opened through the entire radius, i.e. from fiber surface to near its center, for gas to access the light field for sensing, as shown in Fig. 1-1. Creating porosity in such a large volume – the entire cladding – takes long time and tends to weaken the fiber's mechanical strength from our experimental efforts in this project.

To address such issue, we examine off-centered core configuration by positioning the core close to the fiber surface, as shown in Fig. 3-13. The cladding is thinner on one side of the core and thicker on the other side.

Under the case where the core is almost at the surface (Fig. 3-14), the cladding is so thin that the light around the core will extend through cladding into the surrounding air. Therefore the interaction between gas and light in the core is automatically guaranteed. (Note: our study will find the optimal approach forward is to combine porous cladding and off-centered core).

For the off-centered core fiber fabricated in-house, the gap between the edges of core and cladding (core-to-air distance) is not small enough to expose enough core mode for interaction with gas, so chemical etching is used to further expose the core mode and for off-centered core sensor fabrication.

Design of off-centered core sensor

For an evanescent field sensor, the degree of interaction depends on the value of power fraction (PF), which is defined as the ratio between the exposed energy and the total mode energy. In the off-centered core fiber, PF is related to the distance between core and air after reducing the cladding thickness. A 2D model of the off-centered core fiber was created in Radio Frequency (RF) module of COMSOL Multiphysics 5.4 to simulate the energy distribution and to accurately calculate PF with different core-to-air distances.

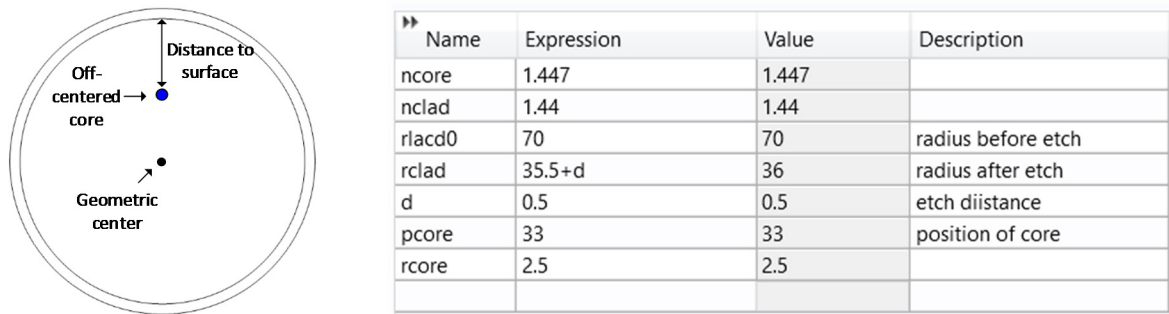


Fig. 3-13. Simulation model settings for off-centered core fiber using Comsol. (Left) the 2D cross-section and (right) the setting parameters.

To derive accurate relationship between PF and core-to-air distance as well as directly observe mode energy distribution change with different etching lengths, an off-centered core fiber model was created whose geometric settings are shown in Fig. 3-13. The simulation model had an eccentric core with a radius of 2.5 μm and an original core-to-air distance of 34.5 μm . Cladding radius was set to 70 μm before etching and an outer air layer was added outside the whole fiber considering the real implementation of the guiding theoretical situation. The refractive index of the core and the cladding was set as 1.447 and 1.44 respectively while the operated wavelength was 1650 nm. As the goal for simulation is to evaluate how energy distribution and the power exposure change with different etching depth, a core-to-air distance d between 0 μm to 5 μm were simulated and analyzed. When d became 0 μm where the core was already in contact with the outside air, the PF would be the largest and presents the sensitivity limit for this model.

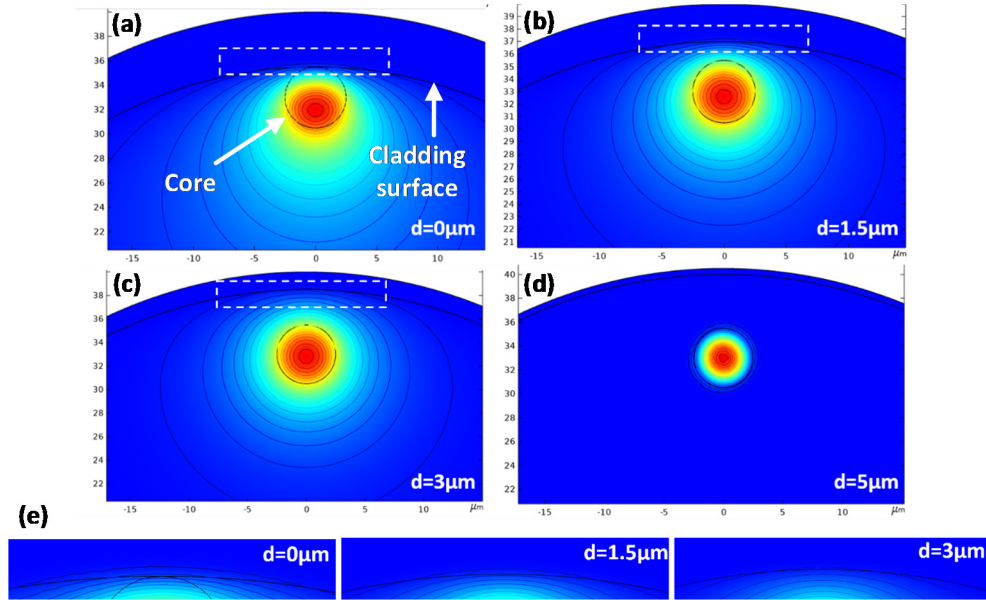


Fig. 3-14. Simulated energy distribution results when gap distance is 0 μm , 1.5 μm , 3 μm , 5 μm separately (a-d). (e) Amplified region of white boxes in (a)-(c).

Fig 3-14 presents the energy distribution around the core section when distance d was 0 μm , 1.5 μm , 3 μm and 5 μm . The black circle in each figure shows the physical position of core, while the different colors from red to blue show different energy level from high to low. Energy contour is also drawn inside Fig. 3-14 to show more clearly whether the electromagnetic field is exposed. The distribution around the cladding boundary circled by dashed rectangle is magnified and shown in Fig. 3-14 (e). As indicated in Fig. 3-14, the energy leakage will appear when the d is less than 5 μm . And the deeper the etching is, the more energy would be exposed to air. Another phenomenon shown in the mode energy distribution results is the slight displacement of mode energy center and deformed distribution contours. As shown from Fig 3-14 (d) to (a), when d is decreased and more evanescent wave intends to leak outside the fiber, the mode center will gradually move inward the fiber trying to compensate for the increasing losses. The deformed contour is also a sign of compensation. For a normal energy distribution around the core section, such as in the case of 5 μm separation, all contours should be circle shapes with the same curvatures. However, with decreasing distance to air, the contour curvature will gradually increase to approach the cladding one for less exposure. The reason for both displacement and deformation is assumed from the reducing refractive index of outside core region. Because the mechanism for a fiber to guide light is the TIR, light wave “prefers” to stay in higher refractive index area. However, as the etching goes deeper, the outer cladding becomes thinner so that average refractive index outside the core region is smaller and mode energy compensation happens.

To accurately evaluate the sensing ability of the designed fiber, the PF was calculated quantitatively. The values of PF with different core-to-air distance (0-5 μm) are listed in Fig. 3-15. As shown in the curve, power fraction will increase with a reduced distance d which corresponds to the direct results from mode distribution figures. However, the fraction change associated with distance is not a linear relationship, but better fitting to a logarithm function when d is greater than 0 μm . When the core-to-air distance is etched

below 0.5 μm , PF shows a sudden increase and can reach up to 0.78% in an ideal occasion.

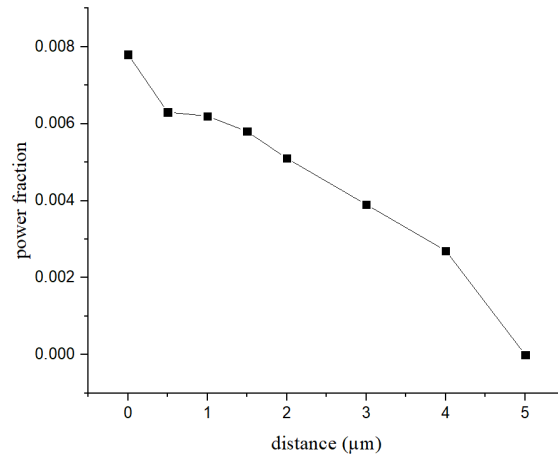


Fig. 3-15. PF change with increasing core-to-air distance.

Fabrication of off-centered core sensor

Chemical etching was chosen to expose evanescent field and fabricate the sensor because the etching process could be controlled by applying different concentration and duration. For the off-centered core fiber, hydrofluoric acid (HF) was chosen as the dissolving solution. According to the simulation results, evanescent fields will be barely exposed if the distance between core and air is greater than 5 μm . However, when the cladding is completely removed, both core size and core shape will be changed, which may cause additional loss. To fabricate a sensor with reasonable exposed portion of core mode, the etching process should be accurately controlled. Scanning electron microscopy (SEM) is usually used to precisely monitor the dynamic etching process [8-13]. However, the high cost and long time limit its wide usage. Thus, a simple and low-cost on-line etching system was designed to control the etching process with a diluted HF concentration. The system configuration included four parts: a light source with a wavelength at 1650 nm, 3-axis U-bench coupler (FBP-A-FC, Thorlabs) composed of two adjustable FiberPort collimators (PAF-X-7-C, Thorlabs), a Teflon groove container with a 13 cm inner diameter, and a power meter (Fig. 3-16). Two sensor samples with different lengths, 10 cm and 40 cm, were fabricated by the system. By monitoring the change in output power with etching time and comparing the core-to-air distances at different time points, etching procedure can be established.

A laser pulse with 5 mW power was excited by a laser driver and controlled by a temperature controller. The light was then coupled into the U-bench coupler through a single mode fiber. The coupled output power was connected to the off-centered core fiber with a maximum coupling efficiency of 60%. After removing fiber coating using sulfuric acid, a middle piece of the eccentric core fiber was winded inside the Teflon groove. To reduce surface roughness and operating difficulty, the HF used was diluted to 25% to extend etching duration. Then, the other end of the fiber sample was well polished and connected to a fast response power meter which can accurately monitor output power change.

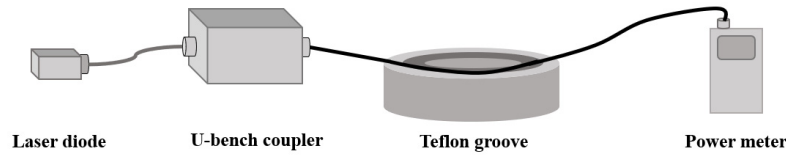


Fig. 3-16. On-line hydrofluoric (HF) acid etching system.

The output power change with time for the 10 cm and 40 cm samples are shown in Fig. 3-17 (a) and (b) separately. For the 10 cm sample, the fiber was taken out of the etching chamber when output power decreased from 3.2 mW to 0.3 mW after 155 min. As for the 40 cm sample, it had a 2.5 mW voltage output before etching while only 0.78 mW was detected at 180 min. Despite the different etching time and power loss, both curves show the same trend that the intensity slightly fluctuates for most of the etching time and suddenly goes through a rapid drop in the last 5 minutes. The 'rapid drop' period is assumed to be a result of the interaction happening between leaked evanescent field power and surface roughness, which causes significant scattering loss. As the etching goes deeper, larger PF will leak out of the fiber and cause more scattering loss. Then the energy inside the core section will continuously compensate for the lost evanescent field energy to keep the original mode distribution until the etching stops. The final loss for the 10 cm sample and 40 cm the sample was calculated as -10 dB and -5 dB separately. Several on-line etching tests with different immersing lengths were repeated, and all of their output power curves showed the same trend.

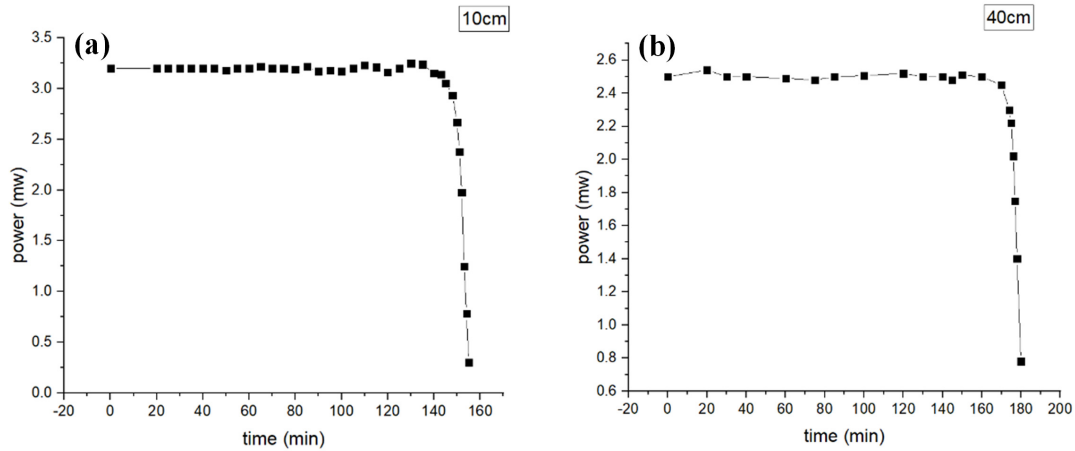


Fig. 3-17. Output power change with etching time. (a) 10 cm sample and (b) 40 cm sample.

After the etching curves under different conditions (time, concentration, etched length, etc.) were analyzed, the next step is to relate the conditions to the distance d after etching and evaluate the etching quality. Cross-section figures with transmission mode at different positions for both 10 cm and 40 cm samples were taken under a microscope, as shown in Fig. 3-18. The cladding diameter in each figure was compared with the unetched fiber to acquire a relatively accurate value of core-to-air distance.

For the 40 cm sample, six images were taken around four different positions on the fiber [Fig. 3-18 (a)]. Although the core seemed to already contact the cladding edge at

all positions, the calibration results showed the accurate distance ranging from $1.5\ \mu\text{m}$ to $2.27\ \mu\text{m}$. As the calculation presents, a small distance between the core and surrounding air was left after etching, with an average value of $1.78\ \mu\text{m}$. The range of 0.77 and the variance of 0.4 indicated good etching uniformity. However, as the distance d should be as small as several micrometers to expose evanescent field and show sensing possibility, the range and variance also showed the appearance of some etching unevenness. As for the $10\ \text{cm}$ sample [Fig. 3-18 (b)], only two images were shown due to the length restriction. The average gap distance was $\sim 4.5\ \mu\text{m}$ but it had a larger loss of $-10\ \text{dB}$. For a long-distance gas sensor, the loss as large as $10\ \text{dB}$ will restrict its practical application. The loss is first assumed to be from scattering as the surface roughness during etching is inevitable. And when more energy interacts with the rough surface, the scattering loss should also be larger. However, as seen from the experimental results, the $10\ \text{cm}$ etching period had a larger loss than the $40\ \text{cm}$ one, which was caused by surface scattering induced by surface roughness after etching.

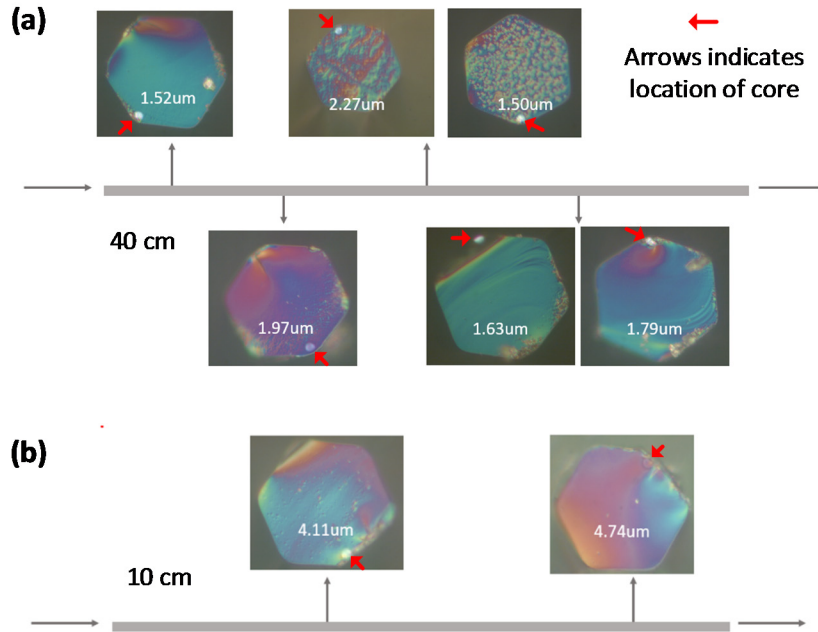


Fig. 3-18. Cross section of different position of off-centered core sensor after HF etching. (a) Etching uniformity for $40\ \text{cm}$ fiber. The average gap length along all the fiber is $1.78\ \mu\text{m}$ with a variance of $0.4\ \mu\text{m}$. (b) Etching uniformity for $10\ \text{cm}$ fiber with a range of $0.63\ \mu\text{m}$. Red arrows mark the location of the core, which is illuminated and appears as a bright spot.

Connection between off-centered core sensor and silica fiber

Because of the off-centered position of the core, the coupling between off-centered core sensor and silica fiber needs fine tuning of the position. Thus, free-space coupling optics was used to couple light signal into the off-centered core sensor as well as receiving its signal output. As shown in Fig. 3-19, the central part of the sensor was mounted within the gas chamber with its ends connected to free space coupling optics with silica input and output fiber. By fine tuning of the fiber end positions and angles, $\sim 25\%$ coupling efficiency can be achieved.

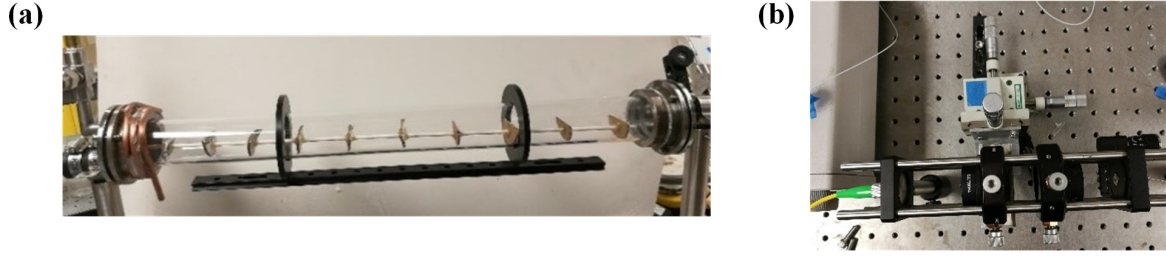


Fig. 3-19. Connection between off-centered core sensor and silica fiber. (a) Off-centered core sensor mounted in gas chamber; (b) The 3-axis free space coupling system for coupling between off-centered core sensor and silica fiber.

3.3. Interrogation system

Equally important as the sensor, the interrogation system is another significant part of the gas sensing system which generates optical detection signal. A conventional interrogation method for distributed gas sensing systems is based on wavelength modulation light source. However, the typical pulse width of such systems are always larger than ~ 500 ns, which greatly compromised the special resolution in sensing. In order to tremendously increase the spatial resolution and achieve quick detection in distributed gas sensing systems, the interrogator in our system used frequency chirped pulse with duration as short as ~ 10 ns for gas sensing, corresponding to ~ 2 m in spatial extent in fiber or spatial resolution.

3.3.1. Theory of chirp generation in DFB laser diode

The emission frequency of DFB LDs is primarily determined by the bandgap of the semiconductor material along with temperature and current density at the active region. Therefore, temperature tuning and injection current modulation are typical methods to obtain frequency chirped output, but they possess different time constants [14]. Temperature tuning is based on the thermal-induced change of bandgap change of semiconductor material and the Bragg wavelength shift of the DFB reflector, which is usually limited by the thermal conductivity of semiconductor material, leading to a frequency tuning time of $\sim \mu\text{s}$.

Current injection to active region will cause emission frequency change through two effects: temperature change through Joule heating effect, and RI change via changing carrier density (current change), thus a wavelength shift described by

$$\Delta\lambda = \frac{\lambda}{n_{eff}} \Gamma_t \frac{\partial n_t}{\partial N_t} \Delta N_t, \quad (1)$$

where λ , Γ_t , n_t , N_t , n_{eff} stands for wavelength, confinement factor of tuning layer, photon density, carrier density and effective refractive index, respectively [15]. Joule heating also results in tuning time on the order of hundreds of ns due to thermal tuning dynamics, whereas the RI change is much faster. Thus, we use injection current modulation for chirp generation to obtain ~ 10 ns pulse duration.

3.3.2. Simulation for chirped pulse generation

Based on the current injection method, a simulation model for chirped output from the LD can be setup with the modification to the LD's rate equations [16] [17]. The following

equations determine the output performance of a DFB LD:

$$\begin{aligned}
 \frac{dN(t)}{dt} &= \frac{I(t)}{qV} - \frac{N(t)}{\tau_n} - g_0(N(t) - N_{thresh}) \frac{1}{1 + \epsilon S(t)} S(t) \\
 \frac{dS(t)}{dt} &= \Gamma g_0(N(t) - N_{thresh}) \frac{1}{1 + \epsilon S(t)} S(t) - \frac{S(t)}{\tau_p} + \frac{\Gamma \beta N(t)}{\tau_n}, \\
 \frac{d\phi(t)}{dt} &= \frac{1}{2} \alpha \left[\Gamma g_0(N(t) - N_{thresh}) - \frac{1}{\tau_p} \right]
 \end{aligned} \tag{2}$$

where $N(t)$, $S(t)$, $\Phi(t)$ stands for electron carrier density, photon density and optical phase, respectively. It should be noted that the output of the laser diode, including its output power and spectrum, can be estimated if all these three parameters can be obtained. The other parameters in the equations are related to the laser diode, where Γ , N_{thresh} , β , α , ϵ , τ_p , τ_n , q , V and g_0 stand for the model confinement factor, carrier density at transparency frequency when net gain is 0, fraction of spontaneous emission coupled into lasing mode, linewidth enhancement factor, gain compression factor, photon lifetime, electron lifetime, electron charge, active layer volume and gain slope constant, respectively. The value of these factors can be either obtained from the LD manufacturer or evaluated from typical values. It can be seen from the equations that the output pulse as well as its spectrum can be modulated with the influence of the input driving current $I(t)$, which describes the feasibility of chirp generation with current injection method.

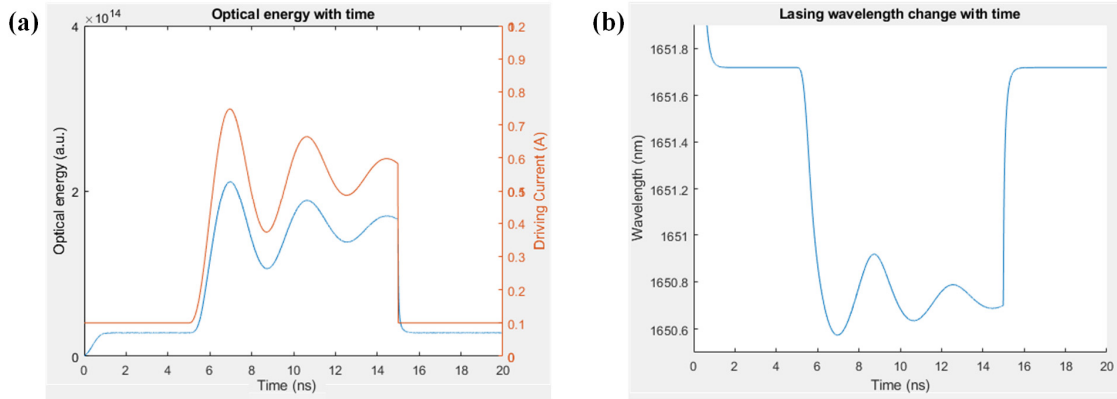


Fig. 3-20. Simulation results of the chirped output from the DFB LD. (a) Output pulse shape (blue line) with the driving current shape (red curve); (b) Temporal spectrum.

As shown in Fig. 3-20, with the modulated driving current pulse, pulsed output can be obtained from the LD. Meanwhile, due to the inevitable current ringing effect and limited responding bandwidth of the pulse generator when operating in ~ 10 ns pulse output, the driving current cannot maintain a perfect flat top, which will then result in a fluctuating oscillation on the amplitude of the optical pulse with the same trend. Furthermore, the output temporal spectrum (lasing wavelength with time) also indicated a change of wavelength under the varying optical power amplitude, which confirmed the generation of frequency chirp.

However, this simulation results did not consider the temporal filtering effect induced by the limited responding bandwidth of the current driving equipment and the

photodetector, which reduced the accuracy of this simulation model. Thus, we added the filtering effect induced by limited bandwidth on both driving current and optical power detection part to improve this model. The bandwidth and other necessary parameters applied in the model are obtained from the real equipment used to generate and detect the chirped pulse in the next section.

As can be seen in Fig. 3-21, after consideration of limited bandwidth, the sharp rising and trailing edge of the pulse become gradual change, and the pulse amplitudes of the peaks and valleys on top of the pulse also fluctuate, which also influence the wavelength distribution in the chirped pulse.

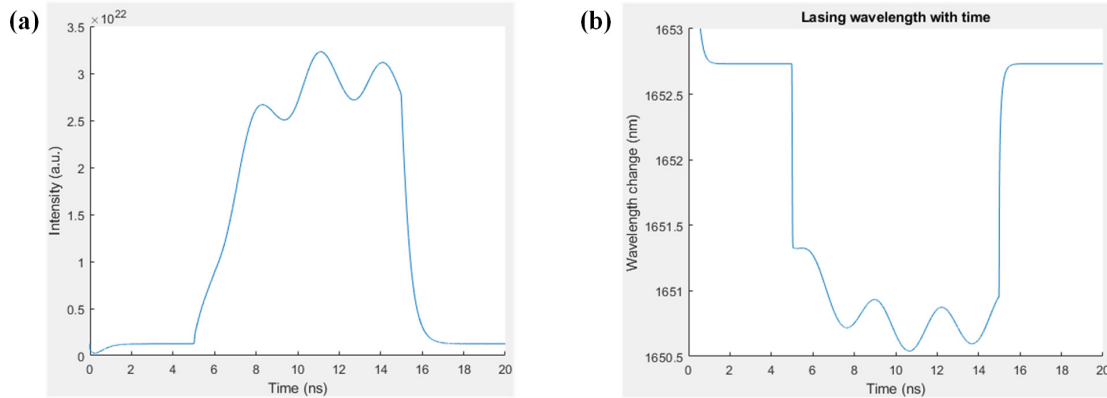


Fig. 3-21. Simulation results of chirped pulse after considering limited bandwidth. (a) Output pulse shape; (b) Temporal spectrum.

As a further expansion of this simulation model, the absorption of methane is added into it to simulate the non-uniform absorption within the chirped pulse, which is expected in our design and used for methane concentration sensing. The simulation result is shown in Fig. 3-22. Methane's absorption peak located at 1650.9 nm with an absorption band of ~ 0.08 nm is added into the model. When assuming a 100% power absorption at the absorption peak, the pulse shape is changed to Fig. 3-22 (b) without considering the bandwidth-induced filtering effect of PD. However, the limited bandwidth of PD is an unavoidable factor that will significantly influence the temporal shape of the pulse, especially when detecting ultra short pulses with duration of ~ 10 ns. After adding the responding bandwidth of PD, the detected pulse shape became the blue curve in Fig. 3-22 (a). The filtering effect of PD added an averaging effect on the pulse temporal envelope that slowed down the sharp change at the edge of absorption-caused depression, which also expanded its width. This phenomenon is confirmed in our experimental results.

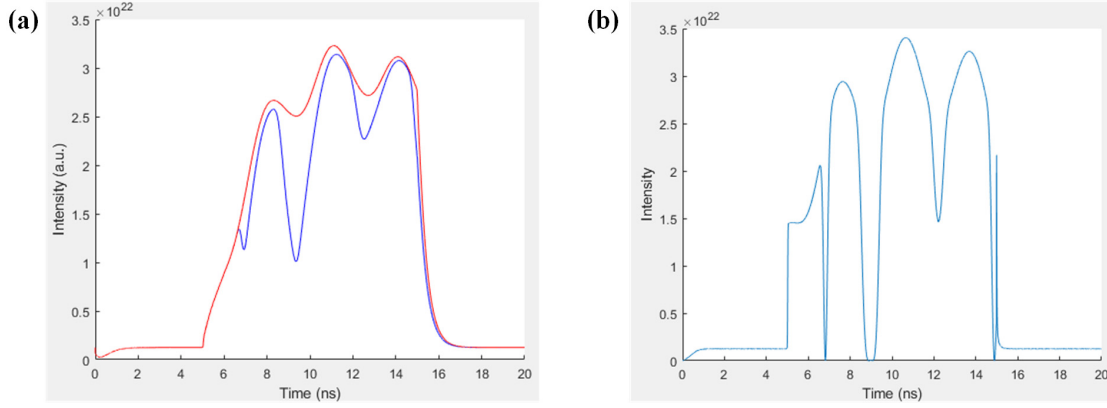


Fig. 3-22. Shape change of the chirped pulse after methane absorption. (a) Pulse shape before (red) and after (blue) methane absorption after consideration of PD bandwidth; (b) Pulse shape after methane absorption without consideration of PD bandwidth.

3.3.3. System for chirped pulse generation

The configuration of LD's driving system is schematically illustrated in Fig. 3-23. A voltage pulse generator (AVMN-C, AVTECH) triggered by a function generator (HDG1022A, Hantek) was used to generate voltage pulses with a duration of ~ 14 ns. The voltage pulses were then coupled into a bias-T module (T1G, Thorlabs) to be changed into current pulses. Meanwhile, a DC current supply (Model 505, Newport) was also added to the bias-T as a DC bias in order to pump the LD slightly below lasing threshold. The output from the bias-T was a ~ 14 -ns pulse train with a peak current of 110 mA and a 17.5 mA DC current bias. This pulse train was then coupled into the input port of a DFB LD (BF14-DFB-1650, Fspotonics) as the driving current. With such a rapidly changing driving current, the output frequency within the pulse changes with time, thus achieving frequency chirp. During the injection current modulation, a TEC temperature controller (TED2000C, Thorlabs) was connected to the LD to stabilize its temperature and output spectrum. It can also control the central wavelength shift by changing TEC temperature. For methane sensing, the DFB LD was set to operate near the absorption peak at 1650.9 nm [18]. The pulse duration can be tuned by changing the duration of the output from the voltage pulse generator.

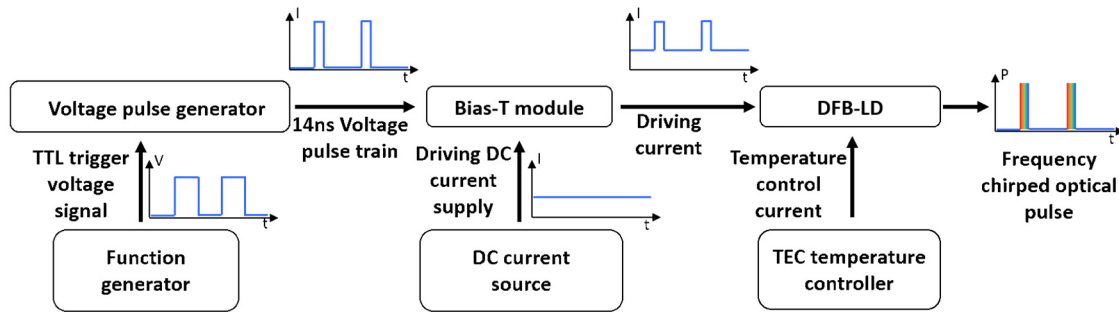


Fig. 3-23. Driving method to achieve ns-pulsed output from DFB laser diode.

The setup of chirped pulse driving system is shown in Fig. 3-24. The LD was fixed on a LD driving mount, its temperature was controlled by a TEC controller. To avoid unwanted energy drop and distortion of RF pulse, the output of bias-t module was directly soldered onto the input pins of LD [19] [20].

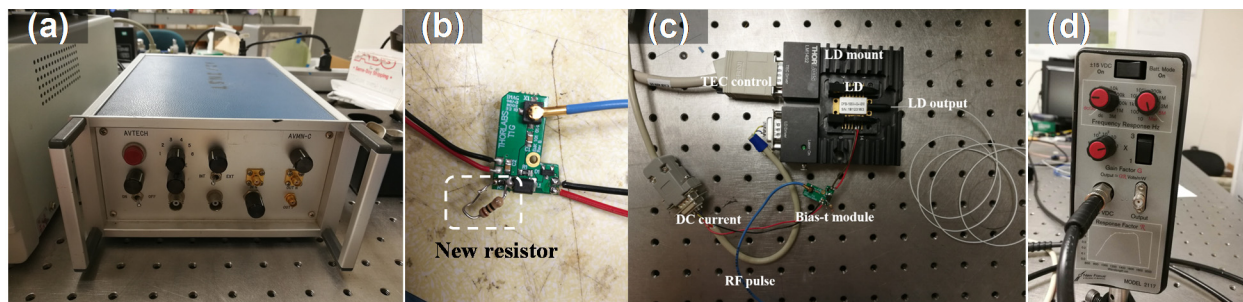


Fig. 3-24. Chirped pulse driving system setup. (a) Pulse generator. (b) Bias-T module. (c) Mounted laser diode with fiber pigtail. (d) High-speed photodetector.

In the experiment, frequency chirped pulses with a width of ~ 10 ns and central wavelength at 1650.5 nm were generated. To confirm the generation of frequency chirp, the pulse shapes after propagation through nitrogen and methane were measured and shown in Fig. 3-25.

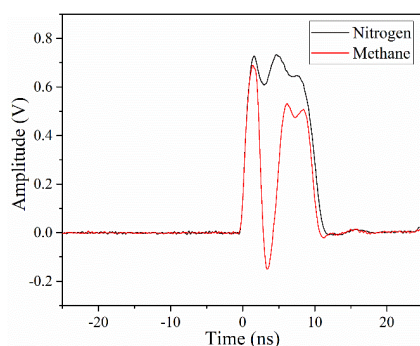


Fig. 3-25. Output pulse when chamber filled with nitrogen and methane.

The pulse shape keeps unchanged after propagation through nitrogen because no absorption peak of nitrogen exists at ~ 1650 nm band. Meanwhile, a clear amplitude depression can be observed at the center of pulse while the edges of pulse experienced much lower amplitude loss and smaller shape change after propagation through methane. This result is caused by the non-uniform wavelength distribution within the pulse in time domain as a result of frequency chirp. Light component at the absorption wavelength experienced large amplitude loss and caused depression in the center of pulse, while the edges got much less amplitude drop because the wavelength was away from absorption line of methane. The relatively low change at the edges of pulse can also serve as a calibration to derive the concentration of methane. The reason for the negative amplitude at methane absorption peak is the influence of limited bandwidth of the PD with a too sharp optical power change, which will affect the accuracy of gas sensing results. This issue can be fixed by shortening the total interaction length between light signal and gas and fine adjustments of the LD driving signal.

Moreover, it should also be noted that because of the variation in fiber material and core size when the free space sensing cavity is replaced with different kind of fiber sensors, the shape of chirped pulse as well as its duration may change as a result of the changed dispersion and attenuation of the fiber sensors.

3.3.4. Characterization of chirped output

As is shown in Fig. 3-26, a Mach-Zehnder interferometer was set up to observe the frequency chirp. The output from laser diode was evenly separated into two arms by a 3 dB coupler. One arm was a piece of singlemode fiber as sample arm and the other added a time delay line which introduced 2 ns of time delay as reference arm. The output of the two arms were then combined with another 3 dB coupler. The

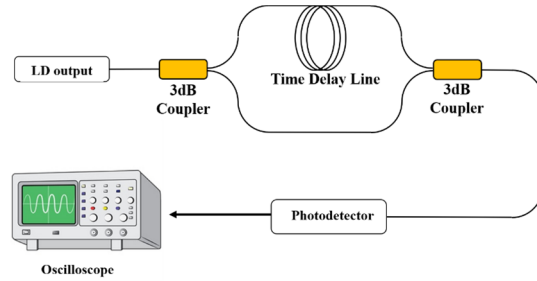


Fig. 3-26. Experimental setup for chirp observation system.

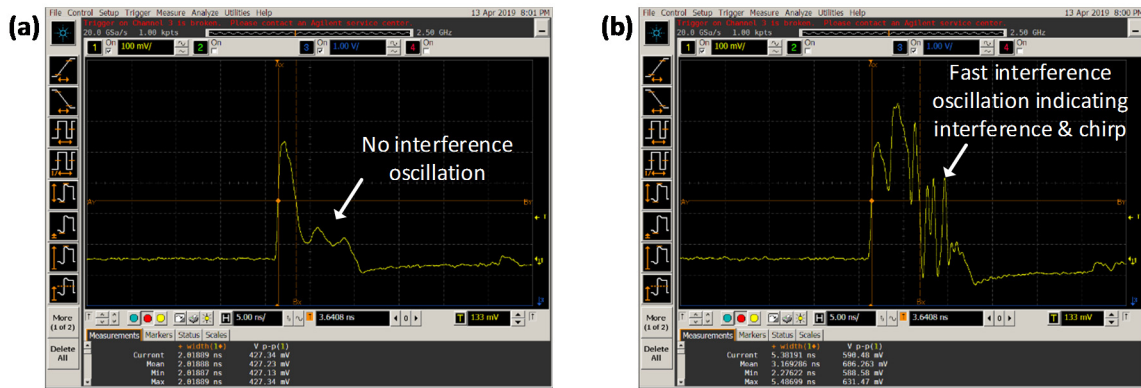


Fig. 3-27. Observation of frequency chirp. (a) Pulse at output of reference arm with no interference; (b) Pulse interference at output indicating chirp.

The measured results are shown in Fig. 3-27. The output from reference arm is shown as in Fig. 3-27 (a). Combining the outputs from these two arms, light interference was observed and had a pattern shown in Fig. 3-27 (b). The combined output showed clear interference peaks, which is a strong indication of frequency chirp, confirming the chirped output.

Meanwhile, although the wavelength distribution within the temporal envelope is complicated, tuning of the wavelength can be achieved by changing the operation temperature of the LD through TEC tuning. As shown in Fig. 3-28, the wavelength shift within the chirped pulse through TEC temperature changing can be confirmed with the shift of methane absorption peak at 1650.9 nm [21].

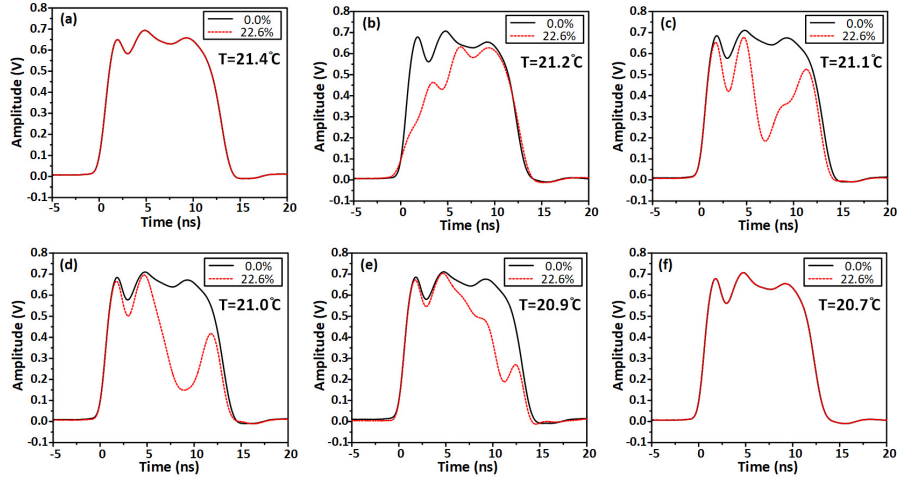


Fig. 3-28. Wavelength tuning in chirped pulse through TEC tuning.

The shape changes of the chirped pulses after passing through methane-nitrogen gas mixture at different TEC temperatures are shown in the figure. The methane concentration is either 0 (pure nitrogen) or 22.6%. First, it can be seen that, when methane concentration is 0%, pulse shapes are nearly identical. Using an optical spectrum analyzer, we observed a central wavelength shift from 1651.2 to 1650.8 nm with a bandwidth of 0.08 nm when tuning the TEC temperature from 21.4 to 20.7 °C.

Next, this shift was directly visualized in a qualitative way using 22.6% methane to generate absorption within the pulse. In Fig. 3-28 (a), the pulse wavelength is still outside of methane absorption band at 1650.9 nm. The shape of the 22.6% methane curve (red) is hence identical to that of 0% methane (black). As TEC temperature increases in Fig. 3-28 (b)-(f), the absorption band emerges from the leading edge (left) of the pulse and gradually moves toward the trailing edge (right), and eventually shifts out of the pulse again. This is consistent with the measurement of the optical spectrum analyzer that the average (central) wavelength of the pulse shifts as temperature changes. This effect can be used to position the absorption region within the pulse if needed. For example, it may be beneficial for the absorption region to locate near the middle of the pulse to capture the full shape of the absorption line, as shown in Fig. 3-31 next.

4.0 Research Findings and Accomplishments

In this section, we discuss the research results and findings in gas sensing evaluation. After the fabrication of fiber gas sensors and the design of the interrogation system, a gas sensing system was setup and three configurations were evaluation: free space transmission (Section 4.1), porous clad gas sensor (Section 4.2) and off-centered core gas sensor (Section 4.3), followed by a summary of research accomplishments.

4.1. Gas sensing based on free space transmission for interrogation evaluation

The free-space transmission spectroscopy is the simplest method for gas sensing based on simply shooting the detection signal through the mixed gas in gas chamber. Because of its high interaction between the detection signal and gas, this system is a good way to test the new interrogation technique.

Experimental setup

The transmission gas sensing system was setup as shown in Fig. 4-1. The chirped pulses were collimated out of the LD's output fiber into a gas mixture, and were then coupled back into a single mode fiber for detection by a fast photodetector (FPD 510, MenloSystems) and an oscilloscope (DSO90254A, Agilent). The collimation and coupling optics were sealed in a gas chamber filled with controlled methane-nitrogen mixture. The total interaction length between the pulse and gas mixture was 11 cm.

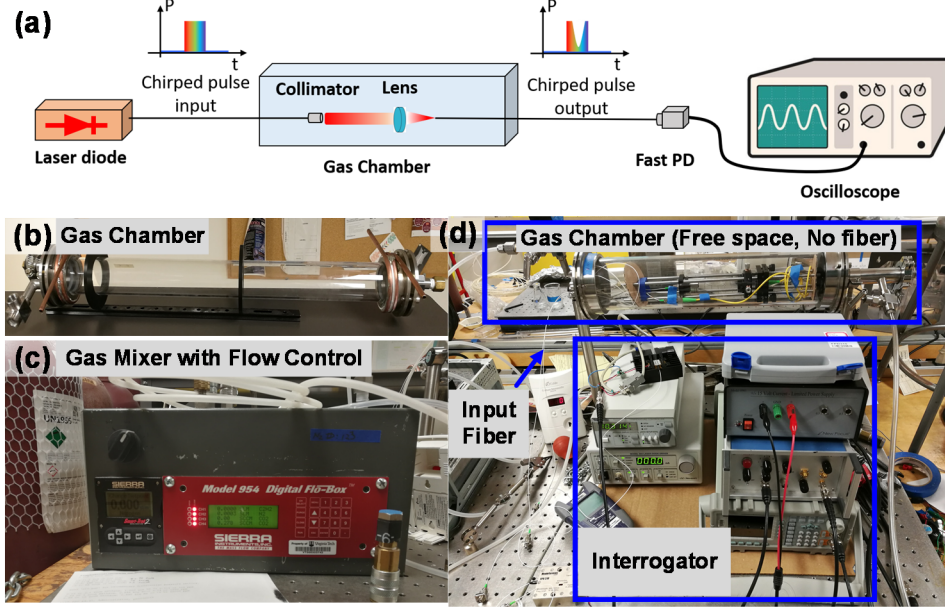


Fig. 4-1. Gas sensing system based on free space transmission. (a) System schematic. (b) Gas chamber glass tube. (c) Gas flow mixing and control unit. (d) System picture.

Methane concentration and calibration of gas mixer

The nitrogen-methane mixed gas flow in the gas chamber is controlled by a gas mixer which controls the methane concentration. Thus, the accuracy of the reading of gas mixer directly affects the gas sensing accuracy. To calibrate the reading of gas mixer, water replacement method was used as shown in Fig. 4-2. The results showed a mismatch between the gas mixer reading and the actual flow rate due to the difference between standard temperature and room temperature. However, the actual gas flow showed good linear relationship with the gas mixer reading, only with small mismatch at very low readings. Thus, precise methane concentrations of the mixed gas can be evaluated based on this calibration.

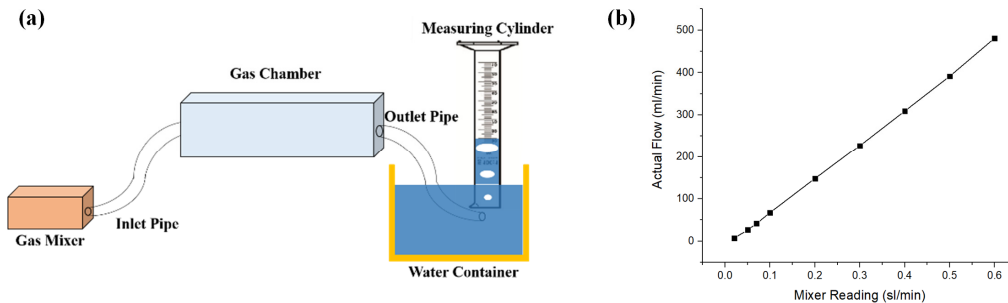


Fig. 4-2. Calibration of gas mixer flow rate with water displacement method. (a) Water displacement method for calibration; (b) Actual gas flow with the reading of gas mixer.

Free-space transmission gas sensing results

The pulse shape for methane concentration between 0% and 22.6% was shown in Fig. 4-3 (a). Each curve represents an average of 150 pulses. As the concentration increases, increasing absorption can be observed over the entire pulse with the strength at 9.0 ns being much greater than other positions.

To accurately quantify the absorption, the pulse amplitude change due to absorption must be isolated and analyzed alone. To this end, we note that the amplitude of the pulse is impacted not only by absorption, but also by the inherent pulse amplitude variation. For example, even for 0% methane with no absorption, the pulse amplitude varies at different time points, forming an inherent amplitude envelope of the pulse. This envelope is on top of additional absorption effect and must be removed (normalized).

To do so, all pulses are normalized to (divided by) the pulse shape with 0% methane (pulse envelope) to cancel its effect, and the results are pure absorption-induced change, as shown in Fig. 4-3 (b). The high absorption at 9.0 ns is caused primarily by a high concentration of spectral component around the 1650.9 nm methane absorption peak. As the wavelength shifts away from this peak, other time points show less absorption.

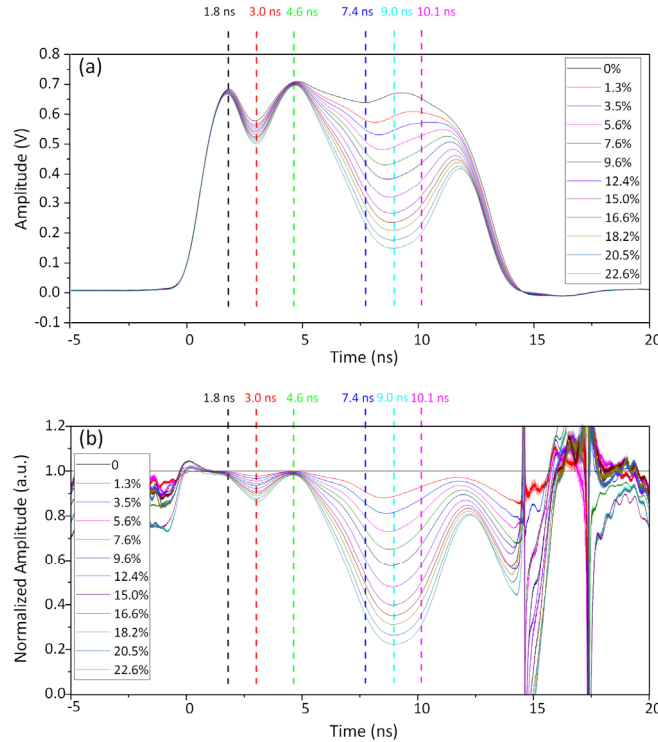


Fig. 4-3. Pulse shapes and normalized pulse shapes with different methane concentrations. (a) Pulse shapes after propagation through gas mixtures. (b) Pulse shapes normalized to that of 0% methane.

To quantitatively examine the response, normalized amplitude at 1.8, 3.0, 4.6, 7.4, 9.0, and 10.1 ns under different methane concentrations are plotted in Fig. 4-4. These time points are marked in Fig. 4-3, including peaks, valleys and major slopes of the pulse profile. The results for 7.4, 9.0, and 10.1 ns show a clear exponential relationship between the normalized amplitude and concentration, following the Beer-Lambert law [22]. The amplitude changes at 1.8, 3.0, and 4.6 ns are rather gradual with small slopes due to the

much smaller absorption at these positions. This could be the result of either a weak absorption coefficient or a small percentage of the on-absorption-peak spectral component.

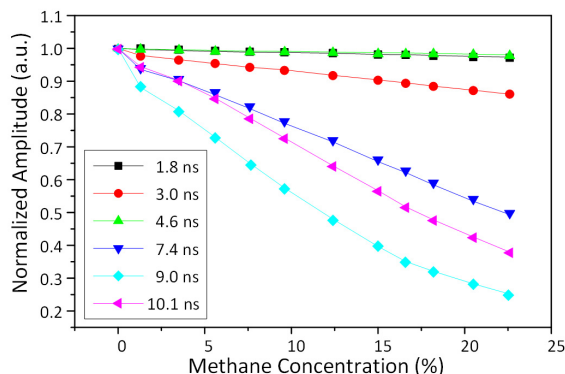


Fig. 4-4. Normalized amplitude changes at different positions of pulse with methane concentration.

The varying degrees of absorption within the pulse and the excellent pulse stability offer an opportunity for intra-pulse self-calibrated measurement. Specifically, when compared with the amplitude drop at 9.0 ns, the attenuation at 4.6 ns is significantly smaller, especially for higher methane concentrations. Therefore, by taking the amplitude ratio between these two points in the same pulse, intra-pulse self-calibration can be achieved. Fig. 4-5 shows the change of this ratio with methane concentration, which fits well to an exponential curve. This method provides a self-calibrated sensing approach that does not need the measurement of a standard gas sample for calibration (baseline).

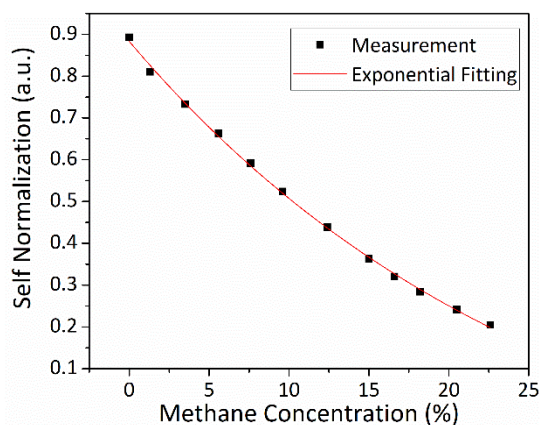


Fig. 4-5. Change of amplitude ratio of 9.0 ns to 4.6 ns with methane concentration for intra pulse calibration.

We also evaluated system stability and detection sensitivity. To this end, the normalized amplitude of the 9.0 ns absorption peak was monitored, as shown in Fig. 4-6. The gas chamber was first filled with pure nitrogen, followed by 1.3% methane mixture injected at 0 min at a flow rate of 0.5 L/min. Immediate decrease in signal amplitude was observed followed by stabilization after 30 min. To better suppress noise, a parabolic fitting was used around the absorption dip to find the minimum. The relative standard deviation of this signal for pure nitrogen is 0.02%, or 25 ppm of methane given that the signal changes

10.1% over a 1.3% increment in methane concentration. This represents the gas detection sensitivity of the system at low concentration at the current level of pulse averaging and source power. At 1.3% methane, the standard deviation deteriorates to 0.04%, which may be largely due to the concentration fluctuation of the gas mixer control.

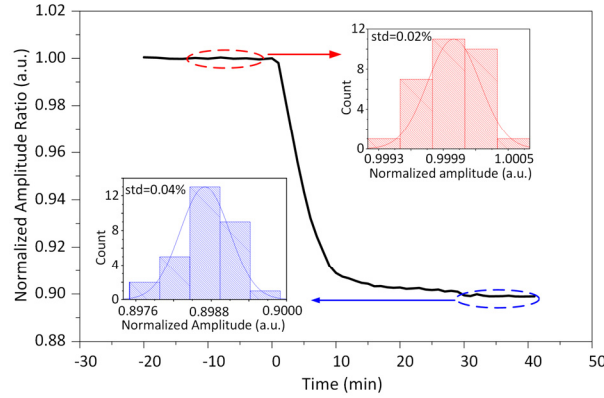


Fig. 4-6. Time trace of normalized amplitude at the absorption peak. (Insets: Normalized amplitude distribution for pure nitrogen (red) and 1.3% methane (blue)).

We note that Fig. 4-6 also indicates the slow mixing speed of the gas mixer. It takes minutes for the gas concentration to stabilize. Due to this limitation, we were unable to measure the response time of the sensors. Modification is needed in the future for this characterization.

Inter-pulse calibrated gas sensing with reference time delay arm¹³

As a setup for the potential of self-calibration sensing application, a reference arm with time-delay line was added into the transmission spectroscopy system (as shown in Fig. 4-7). The input frequency pulse signal was separated into two arms with a 50% fiber coupler, where one is coupled into the transmission spectroscopy system as sample arm and the other is coupled into the reference arm. The total length of reference arm and sample arm were carefully controlled to make the output pulse from sample arm have a ~ 10 ns time lag comparing with that from reference arm. The pulses from both arms are then combined with another 50% coupler, which was then recorded by an oscilloscope.

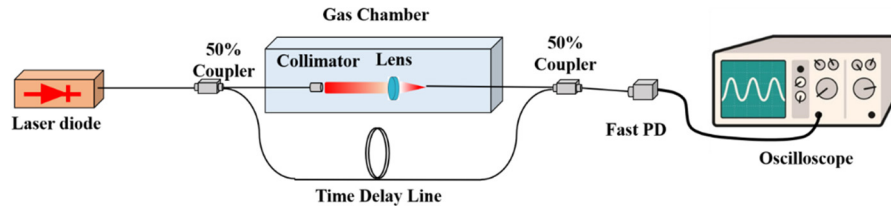


Fig. 4-7. Transmission spectroscopy system with reference arm, similar to the one in Fig. 3-30 but with an additional fiber time delay line.

¹³ Reference time delay arm: This time delay arm is for comparison with the signal pulse through the gas chamber. It provides an absorption-free pulse reference. In the meantime, this additional pulse allows evaluation of the spatial separation of the pulses and thus the spatial resolution of the system.

The measured output is shown in Fig. 4-8. Due to time difference, pulse from reference arm and sample arm had almost no overlap, which prevented shape distortion and interference. Pulse shape from both arms were identical when gas chamber was filled with nitrogen while apparent amplitude drop and shape change of pulse from sample arm can be observed when chamber is filled with methane. The shape change and amplitude drop comparing with those from reference arm can be used as a self-calibrated detection result for distributed gas sensing.

Importantly, each pulse has a temporal duration of 10 ns, which is equivalent to 2 m in spatial extent inside a fiber. Since both pulses are well separated from each other, this demonstrates the spatial resolution of the interrogation system is 2 m.

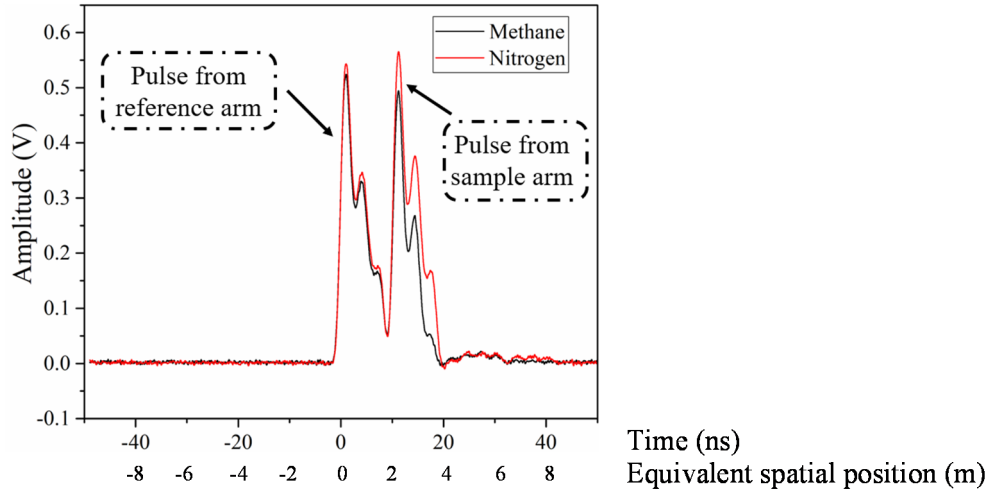


Fig. 4-8. Pulse output from reference arm and sample arm. The x axis is also marked with equivalent spatial location in fiber.

4.2. Gas sensing with porous clad sensor

By changing the free space coupling optics to porous clad sensor in the system demonstrated in Fig. 4-1, a gas sensing system based on porous clad sensor is developed as shown in Fig. 4-9. Due to the length limit of the gas chamber, a porous clad fiber of ~30 cm was cut from long pieces and placed inside the gas chamber.

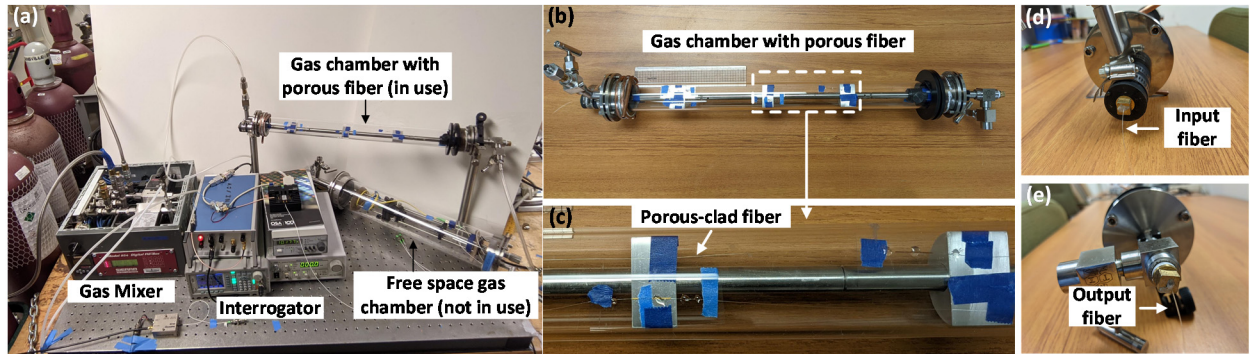


Fig. 4-9. Gas sensing system based on porous clad sensor. (a) Sensing system configuration; (b)(c) Porous clad sensor mounted in gas chamber; (d) (e) Input and output fibers of the gas chamber.

Because both the input and output ends of the porous clad sensor has been connected with silica fiber, the stability and flexibility of the sensor improved comparing with the free-space coupling sensing system. Meanwhile, due to the core size mismatch between the output multimode fiber and input singlemode fiber of the PD, the amplitude of signal decreased as a result of connection loss. Moreover, due to the modal interference and adjusted driving current parameter settings to achieve the best sensing response, the pulse shape of the chirped pulse was slightly changed.

As shown in Fig. 4-10, methane's absorption peak was moved to the first valley of the chirped pulse through TEC tuning, and the intra pulse reference point was selected to be the amplitude of the first peak. For better recognition of the sampling point and the reference point, pulse alignment, noise subtraction and curve fitting were conducted in the data processing, and the fitted amplitudes of the sampling point and reference point are marked as red dots in Fig. 4-10 (b). There are 20 measurements as well as the fitted results shown in the figure, which overlapped perfectly, indicating the effective improvement on the measurement stability and the accuracy of the sampling point and reference point data extraction. After the data processing, the intra-pulse calibrated ratio has a fluctuation lower than 1% under the gas flow in chamber.

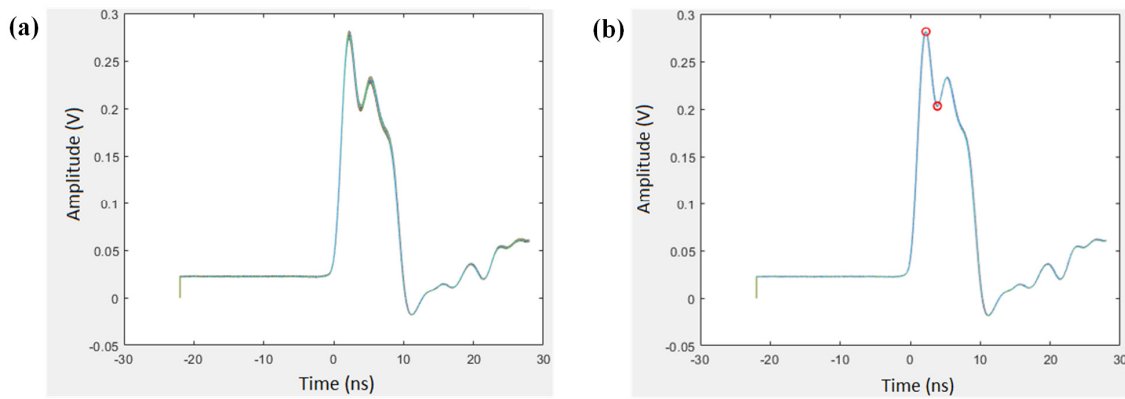


Fig. 4-10. Pulse shape of the detection signal for porous clad sensor. (a) Stability analysis of the chirped pulse with pure nitrogen; (b) Aligned pulses and its sampling points and reference points through data processing. Note that the pulse duration is 10 ns, the same as those in Fig. 3-36 and indicating a spatial resolution of 2 m.

Next, by changing the concentration of methane in the mixed gas flow in gas chamber, full concentration range change of intra-pulse calibrated ratio is measured and shown in Fig. 4-11. For a higher response to methane concentration change, the amplitude of 100% methane concentration absorption valley was subtracted before taking the ratio. Comparing with the free-space coupling sensing system, the system with porous clad sensor can cover a wider sensing range from 0% to 100%, which effectively expanded the application scenarios of the system. Moreover, the linear fitting of the measurements is also shown in the figure, showing good match with the measurements along the full measurement range. The linearity between the measurements and methane concentration has a great improvement comparing with the free space transmission spectroscopy system due to the smaller portion of signal power interaction with the ambient environment.

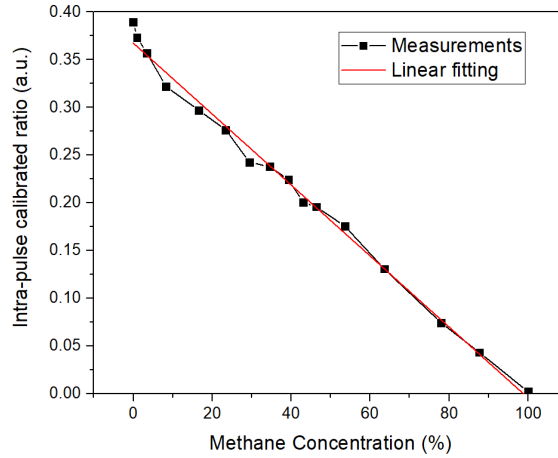


Fig. 4-11. Intra-pulse calibrated ratio change with methane concentration and its linear fitting.

4.3. Gas sensing with off-centered core sensor

The sensing results for the 40 cm and 10 cm off-centered core sensors are shown in Fig. 4-12, where (a) and (c) are the amplitude change within the whole pulse, (b) and (d) show the results within intercepted time period for detailed analysis. Both nitrogen and methane curves represent a 100% concentration with an average of 150 measurements. Compared with Fig. 4-12 (a) and (c), the most evident pulse change both appears during 5 ns - 9 ns and the 40 cm sample has a better detection ability than the 10 cm one. To evaluate their performance precisely, the signal between 5 ns and 9 ns for both samples was drawn in Fig. 4-12 (b), (d), respectively. For the 10 cm sample which has an average gap distance of $\sim 4.5 \mu\text{m}$, the largest amplitude difference between two curves is 0.02 V at 7 ns, while for the 40 cm sample whose gap length is $\sim 1.7 \mu\text{m}$, a more evident signal difference of 0.04 V shows at 8.3 ns.

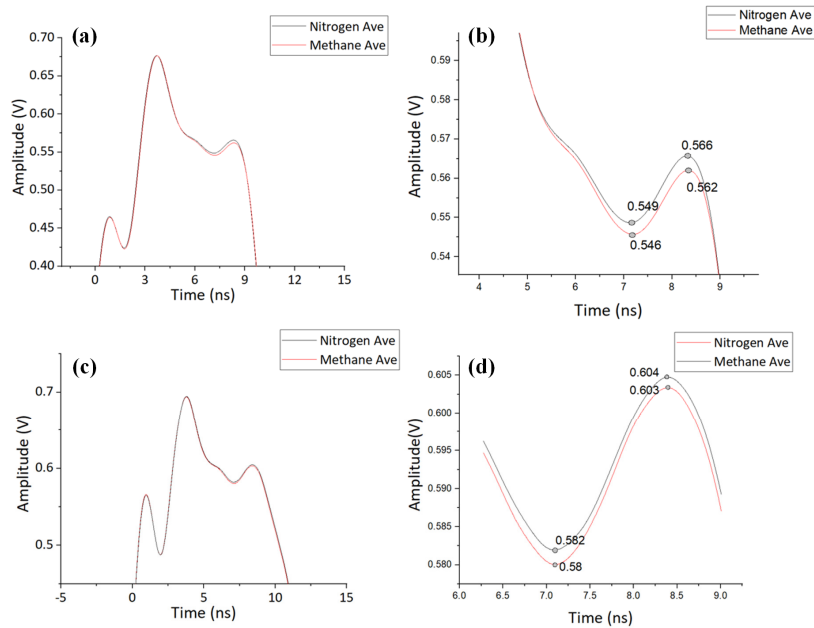


Fig. 4-12. Pulse change with 40 cm (a) (b) and 10 cm (c) (d) sample separately. Figure (b) (d) are the magnified figures between ~ 5 -10 ns. Numbers in (b) and (d) are values of pulse amplitude at corresponding points.

Based on the experiment results and discussions, the sensitivity for off-centered core sensor has great potential for further improvement and to reach to a relatively high sensitivity at about 1%. However, the current response cannot match with the performances from the free space coupling system and the porous clad sensor system, so it is not the best choice worth further evaluation of its sensing performance with lower methane concentration. Once the detection resolution is increased, the possibility to fabricate a multiplexed sensor with high mechanical strength and low cost can be enhanced. Furthermore, the easy sensor fabrication procedure and low transmission loss of the off-centered core sensor will exhibit its great potential in distributed gas sensing systems.

Most importantly, a future combination of off-centered core and porous-cladding fiber could address current challenges in fabrication and performance by reducing fabrication complexity, improving loss performance, and enhancing gas sensitivity.

4.4. Summary of accomplishments

This project has made multiple accomplishments on the novel design of optical fiber-based gas sensors, new mechanism-based optical interrogation system and the development of an optical gas sensing system that will show great potential in hazardous gas sensing for the improvement of mine safety.

- (a) Novel optical interrogation system for gas sensing: We developed a new type of optical interrogation system based on the frequency chirped pulse generated from a laser diode, which suppressed the detection pulse width to ~10 ns to achieve excellent spatial resolution (2 m) and high detection repetition rate. A complete numerical simulation model was setup to characterize the properties of the chirped pulses and provided effective guidance on the modification of chirped pulses to obtain better gas sensing performance.

This is the first technique that will fundamentally enable a successful implementation of high-performance distributed gas sensing. The detailed investigation of the interrogator has convincingly shown its reliable performance in provide targeted detection of hazardous gases in the concentration range relevant to mine safety.

- (b) Novel designs of optical fibers capable of gas sensor fabrication: By exploration and characterization of new glass material combination for fiber, we developed two new designs of optical fiber, BK-7 core/Green Vycor cladding and Ge-doped silica core/fused silica cladding fiber, which are capable of fabrication of porous clad gas sensors and off-centered core gas sensors.
- (c) Novel designs of optical gas sensors: Based on the preceding novel optical fibers, two types of gas sensors with porous clad and off-centered core, respectively, were developed and fabricated. A numerical model was developed and achieved the characterization of optical field distribution along fiber cross section and interaction with ambient environment, which is a powerful tool for exploration of optical fiber-based gas sensor design.

These results are important in that they demonstrate the potential feasibility of a distributed gas sensing system. More importantly, the detailed fiber characterization enables us to understand the key issues of design and fabrication. This will be significant in helping us in more advanced designs of the fiber in the

next steps to lower loss and enhance sensitivity, which are critical for realizing our long term goal of distributed gas sensing in underground mines.

- (d) Setup and evaluation of multiple gas sensing systems: Based on the preceding gas sensors and interrogation system, we achieved the design and setup of gas sensing systems with free space transmission spectroscopy, porous clad sensor, off-centered core sensor and reference time delay arm, respectively. The experimental results proved the effectiveness of the interrogation system and the fiber gas sensors for methane concentration sensing. The system based on free space transmission spectroscopy achieve sensing sensitivity of 25 ppm. The porous clad sensor-based sensing system achieved intra-pulse calibrated, full range-methane concentration sensing. The results of the system with the reference time delay arm proved the effectiveness of inter-pulse calibration and the potential of distributed gas sensing.

5.0 Publication Record and Dissemination Efforts

Under the support from the Alpha Foundation for the Improvement of Mine Safety and Health, Inc., this study has disseminated and is continuing to disseminate the knowledge generated in this research through the following publications and presentations.

Journal publications:

1. G. Shi, D. Homa, X. Su, G. Pickrell, A. Wang, and Y. Zhu. (2020). 12-ns Frequency Chirped Pulse for Self-Calibrated Gas Sensing. IEEE Photonics Technology Letters.

Conference presentations:

1. M. Barros Daza, N. Ripepi, G. Shi, Y. Zhu, G.R. Pickrell, and K. Luxbacher, "Applicability of Distributed Optical Fiber Sensing for a Longwall Face," 2020 SME Annual Conference & Expo, Feb 2020.
2. G. Shi, D. Homa, X. Su, G. Pickrell, A. Wang, and Y. Zhu, "Frequency Chirped Pulse-Based Methane Sensing with Inter-Pulse Calibration," Accepted for presentation in the 27th International Conference on Optical Fiber Sensors, June 2021.

Manuscripts in-progress:

1. M. Barros Daza, N. Ripepi, G. Shi, Y. Zhu, G.R. Pickrell, and K. Luxbacher, "Applicability of distributed optical fiber sensor for a longwall face."
2. G. Shi, and Y. Zhu, "A numerical model of chirped pulse generation from DFB LD."

MS (Master of Science) thesis:

1. X. Su., "Design and Evaluation of Off-centered Core Fiber for Gas Sensing." Virginia Tech, 2020.

6.0 Conclusions and Impact Assessments

In this section, we assess the outcome of the technology development, the challenges ahead and solutions, as well as the potential impact in practical applications.

Technology assessment

The two major components of the system, i.e. the interrogator and the fiber sensor, have reached different levels of development at the conclusion of this project. For the chirped pulse interrogation technique, we have well established its feasibility for distributed gas sensing and fully demonstrated its superior performance. This is the first technology that has demonstrated such capability. Although full validation of sensing fiber feasibility still needs more research, we have made significant progress in its development. Hundreds of meters of fibers have been drawn and can be made much longer if needed. Both porous-clad fibers and off-centered core fibers have been investigated in detail for their material and optical properties. Single sensors made from these fibers have demonstrated gas sensing capability. Through the research, much has been learned about the challenges and the potential path forward, as discussed below.

In evaluation of the overall performance of the combined components, the system can deliver a methane sensitivity at 100 ppm level, well sufficient for detecting small concentration change (~1-2%) at the onset of potential hazardous events. The sensitivity remains uniform at any concentration level from 0% to 100%. The spatial resolution is 2 m as decided by the duration of the pulse (10 ns). Further experiments have shown that the pulse duration can be as short as 6 ns using existing hardware, suggesting a potential resolution of 1.2 m or better if higher performance hardware is used. Time response of the sensors were not investigated due to limited gas mixing speed inherent in the system. Finally, the all optical implementation of the sensing system provides strong justification for meeting permissibility requirements in underground mine applications.

Challenges and potential solutions

The main challenge in full technology demonstration lies in the optical fiber. In particular, minimizing light loss (attenuation) has been identified as a key area of focus. Low loss sensors will allow sufficient light to reach downstream sensors for adequate interrogation.

Many factors can affect signal loss, such as impurity in the glass material, quality of fiber drawing and processing, thermal/chemical treatment, and fiber connections. There are also different approaches to address these challenges. Direct improvement in each of these areas is certainly the most straightforward. Yet the approach mostly likely to be successful is innovative fiber design to lower the requirement in these areas. For example, by integrating the porous-clad and off-centered core concepts, thermal and chemical treatment time and strength can be much reduced. Arranging porous glass and low loss glass or polymer in custom patterns in the fiber cladding may also minimize loss while maintain sensing capability.

On the interrogator side, further sensitivity improvement will also help lower the requirement in fiber development. To this end, we plan to employ wavelength modulation spectroscopy in the interrogation as discussed in future work.

The research efforts in this project have offered tremendous insights into these areas and have strongly pointed directions for future development towards low-loss, long-span sensing in underground mines.

Practical considerations in future applications

Envisioning a practical, full product in the future, we believe the system will consist of an interrogator box connected to a long stretch of fiber cable, similar to a previous single-point gas sensing system that has been granted MSHA experimental permit and tested in mine environment, as shown in Fig. 6-1. The box can be placed at a safe location or even above ground. A distributed sensing system will feature a much longer fiber cable, potentially hundreds of meters or even kilometers. The sensing fiber, roughly $\sim 200\ \mu\text{m}$ in diameter, will be protected inside layers of sheathing, which provide mechanical protection during handling and operation. It will also feature open access channels for gas to interact with the sensors. Particle filter layers will keep contamination from entering the optics. These are some key practical considerations in future product development.

Fortunately, numerous optical fiber cables are routinely packaged and protected when used in real world environment, such as those for optical telecommunication. Many existing materials and techniques can be readily applied in building our sensing cables.

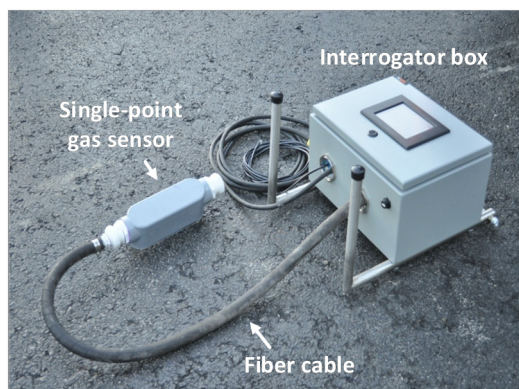


Fig. 6-1. A previous single-point fiber gas sensor with MSHA experimental permit.

Potential impact and applications

Overall, the project successfully built a solid foundation for the proposed technology and pointed directions for future development. It significantly advances the technology toward providing the mining industry a powerful tool for real time monitoring of hazardous gases in order to improve mine safety and health.

In general, the electrically safe fiber-optic sensors are attractive choices for underground mine monitoring for not only gaseous chemicals but also physical parameters such as temperature, pressure and vibration. For example, a distributed methane sensing system can create a methane profile along the entire longwall face. The fiber cable could be installed behind the hydraulic jacks and close to the back of the shields, where power is available and hydraulic cables are also present. Similarly, such sensing cables can also be used for the bleeder ventilation system, such as at the headgate and tailgate entries and bleeder entries. A single sensing cable can conveniently and safely monitor a large number of locations at the same time in these tight spaces with potentially multi-functional outputs.

7.0 Recommendations for future work

The theoretical, simulation and experimental research of the gas sensing platform has proved the excellent effectiveness and potential of using the proposed sensor and interrogation technique to achieve distributed gas sensing with good sensitivity and

stability. More desirable achievements can be expected with further research and development in the following directions:

- (a) Modification and innovation of gas sensor design: Combining porous clad fiber and off-centered core sensor. By fabrication of an off-centered core, partial porous clad fiber, the sensor can potentially achieve excellent mechanical strength, low attenuation, and high gas sensing sensitivity. We have also started exploring other innovative fiber geometries, such as the winged configuration and triangular core fiber shown in Fig. 7-1.
- (b) Sensitivity improvement of the interrogation system with wavelength modulation spectroscopy: By adding a slow-varying driving current to the laser, its output wavelength can be modulated, which can be used to effectively improve the gas sensing sensitivity, potentially by several orders of magnitude.
- (c) Further research on the mechanism of surface roughness-induced attenuation of the fiber-based gas sensors: By building a more complete numerical model for laser propagation in fiber-based gas sensor, we can gain a more insightful understanding of power attenuation in gas sensors, which will guide the modification of gas sensor design to achieve a higher sensitivity.

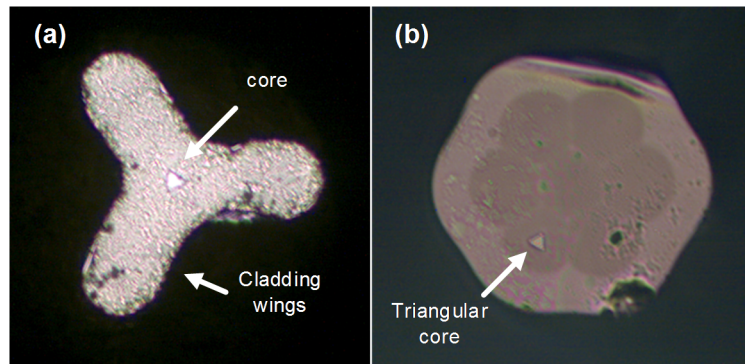


Fig. 7-1. Fibers with (a) winged cladding and (b) triangular core.

8.0 References

- [1] C. Ma, B. Scott, G. Pickrell, and A. Wang. (2010). Porous capillary tubing waveguide for multigas sensing. *Optics letters*, 35(3), 315-317.
- [2] G. Pickrell, B. Scott, C. Ma, K. Cooper, and A. Wang. (2007, October). Stochastic holey optical fibers for gas sensing applications. In *Sensors for Harsh Environments III* (Vol. 6757, p. 67570D). International Society for Optics and Photonics.
- [3] P. G. Kazansky, H. Inouye, T. Mitsuyu, K. Miura, J. Qiu, K. Hirao, and F. Starrost. (1999). Anomalous anisotropic light scattering in Ge-doped silica glass. *Physical Review Letters*, 82(10), 2199.
- [4] S. Chen, J. Ryu, K. Lee, and Y. Zhu. (2016). Swept source digital holographic phase microscopy. *Optics letters*, 41(4), 665-668.
- [5] D. Malacara. (2001). *Handbook of optical engineering*. CRC press.
- [6] M. Artiglia, G. Coppa, P. Di Vita, M. Potenza, and A. Sharma. (1989). Mode field diameter measurements in single-mode optical fibers. *Journal of Lightwave*

- Technology, 7(8), 1139-1152.
- [7] B. L. Scott. (2008). Fabrication and Characterization of a Porous Clad Optical Fiber Gas Sensor (Doctoral dissertation, Virginia Tech).
 - [8] A. Lazarev, N. Fang, Q. Luo, and X. Zhang, X. (2003). Formation of fine near-field scanning optical microscopy tips. Part I. By static and dynamic chemical etching. Review of scientific instruments, 74(8), 3679-3683.
 - [9] H. J. Khashi. (2012). Fabrication of submicron-diameter and taper fibers using chemical etching. Journal of Materials Science & Technology, 28(4), 308-312.
 - [10] A. K. Mallik, A. Kumar, G. Gupta, and A. Bhatnagar. (2012, December). Single mode fiber-optic temperature sensor fabricated using wet etching. In 2012 International Conference on Fiber Optics and Photonics (PHOTONICS) (pp. 1-3). IEEE.
 - [11] Y. Yuan, L. Wang, L. Ding, and C. Wu. (2012). Theory, experiment, and application of optical fiber etching. Applied optics, 51(24), 5845-5849.
 - [12] L. Z. Jiao, D. M. Dong, W. G. Zheng, W. B. Wu, C. J. Shen, and H. Yan. (2013). Research on fiber-optic etching method for evanescent wave sensors. Optik-International Journal for Light and Electron Optics, 124(8), 740-743.
 - [13] I. Goldstein, and A. Chabot. (1966). 7B3-Characteristics of a traveling-wave ruby single-mode laser as a laser radar transmitter. IEEE Journal of Quantum Electronics, 2(9), 519-523.
 - [14] T. L. Koch, and J. E. Bowers. (1984). Nature of wavelength chirping in directly modulated semiconductor lasers. Electronics Letters, 20(25), 1038-1040.
 - [15] G. Morthier, and P. Vankwikelberge. (2013). Handbook of distributed feedback laser diodes. Artech House.
 - [16] J. Gao, X. Li, J. Flucke, and G. Boeck. (2004). Direct parameter-extraction method for laser diode rate-equation model. Journal of lightwave technology, 22(6), 1604.
 - [17] J. C. Cartledge, and R. C. Srinivasan. (1997). Extraction of DFB laser rate equation parameters for system simulation purposes. Journal of Lightwave Technology, 15(5), 852-860.
 - [18] The HITRAN Database [Online], Available: <https://hitran.org/>
 - [19] A. R. Behera. (2017). Diode Laser Spectroscopy for Measurements of Gas Parameters in Harsh Environments (Doctoral dissertation, Virginia Tech).
 - [20] M. T. McCulloch, E. L. Normand, N. Langford, G. Duxbury, and D. A. Newnham. (2003). Highly sensitive detection of trace gases using the time-resolved frequency downchirp from pulsed quantum-cascade lasers. JOSA B, 20(8), 1761-1768.
 - [21] G. Shi, D. Homa, X. Su, G. Pickrell, A. Wang, and Y. Zhu. (2020). 12-ns Frequency Chirped Pulse for Self-Calibrated Gas Sensing. IEEE Photonics Technology Letters.
 - [22] D. F. Swinehart. (1962). The beer-lambert law. Journal of chemical education, 39(7), 333.

9.0 Appendices

N/A.